Trace element partitioning between clinopyroxene and alkaline magmas: parametrization and role of M1 site on HREE enrichment in clinopyroxenes

Céline Baudouin, Lyderic France, Marine Boulanger, Célia Dalou, Jean-Luc Devidal

Contributions to Mineralogy and Petrology
(2020) 175:42
https://doi.org/10.1007/s00410-020-01680-6

Accepted 31 March 2020

Trace element partitioning between clinopyroxene and alkaline magmas: parametrization and role of M1 site on HREE enrichment in clinopyroxenes.

Céline Baudouin[1], Lydéric France[1], Marine Boulanger[1], Célia Dalou[1], Jean-Luc Devidal[2]

[1]Université de Lorraine, CNRS, CRPG, F-54000 Nancy, France

[2]Laboratoire Magmas et Volcans, Université Clermont Auvergne, CNRS, IRD, OPGC, 63178 Aubière, France

***Corresponding author: Céline Baudouin**

E-mail: baudouin.geol@gmail.com

Abstract

Trace element partitioning between minerals and liquids provides crucial constraints on igneous processes. We quantified trace element concentrations in clinopyroxene (Cpx) phenocrysts and their phonolite melt inclusions from the 2007-08 eruption of Oldoinyo Lengai (Tanzania), and report Cpx-melt partition coefficients (*D*) and corresponding partitioning equations for rare earth elements (REE) and high field strength elements (HFSE) in alkaline magmas. Heavy REE (HREE: Er, Tm, Yb, Lu) are enriched relative to middle REE in alkaline Cpx and display a specific partitioning behavior that is characteristic of alkaline systems. HFSE (Ti, Zr, Hf) and HREE have similar *D* values (D_{Hf} = 0.25; D_{Lu} = 0.4) that are significantly higher than MREE (D_{Sm} = 0.06). High D_{HREE}/D_{MREE} are strongly correlated with the high values of D_{Zr} and D_{Hf} relative to the low D_{MREE} values. In this study, REE partitioning between phonolite melt and Cpx is not consistent with standard models assuming incorporation of all REE in the Cpx M2 site, but rather highlights HREE substitution in both the M1 and M2 sites. Here we highlight the preferential incorporation of HREE in the VI-coordinated M1 site, whereas light REE and MREE remain mostly distributed in the VIII-coordinated M2 site. REE partitioning is strongly dependant on Cpx chemistry: the ideal ionic radius and HREE incorporation in the M1 site increase with increasing Fe^{3+} content and decrease with increasing Mg^{2+} and Al^{VI} content. In our study, we focus on alkaline evolved magmas, and update existing models to obtain adequate D_{HREE} for alkaline evolved melts. We provide equations to quantify REE and HFSE partitioning, and HREE enrichment in Cpx, those are based on Cpx major element composition and temperature. We propose a new model based on the lattice strain approach that predicts HREE partitioning between Cpx and alkaline magmas. The knowledge of the melt composition or of the trace element contents is not required to obtain D_{REE} from the new model. An improved parameterization of HFSE partitioning between Cpx and phonolite and trachy-phonolite melts is also provided herein. We eventually discuss the potential implications of those new data on our understanding of REE deposits that are commonly associated with igneous alkaline complexes.

Keywords: partition coefficient; clinopyroxene; HREE enrichment; M1 site; alkaline magmas; REE deposits

Introduction

The trace element contents of minerals and melts are used to identify and quantify igneous processes such as partial melting, equilibrium or fractional crystallization, and melt/rock interactions. Those processes are responsible for local economic concentrations of various metals (e.g., rare earth elements, REE), especially in the case of alkaline igneous provinces, which not only feed some of the most famous volcanoes worldwide (e.g., Vesuvius, Etna, Oldoinyo Lengai, Erebus), but are also associated with numerous critical metal deposits (e.g., Mountain Pass, USA; Ilmaussaq, Greenland). The partitioning of key trace elements (Nb, Ta, REE) along the liquid line of descent and their corresponding enrichment in mineral phases are governed by the amount and chemistry of fractionating minerals, and by the chemistry of the corresponding melts. The partition coefficient quantifies the distribution of a given element *i* between a mineral and a melt ($D_i^{\text{mineral/melt}} = \frac{C_i^{\text{mineral}}}{C_i^{\text{melt}}}$). In the case of alkaline magmas, few partitioning data are available for the various crystallizing minerals (Mollo et al. 2016, 2018; Olin and Wolff 2010; Baudouin & France 2019; Beard et al. 2019).

Clinopyroxene (Cpx) is a widespread mineral in igneous rocks, and has a major impact on the liquid line of descent of the corresponding magmas. In alkaline silicate igneous rocks (syenite, phonolite, nephelinite) and carbonatites (the main REE deposits on Earth), Cpx commonly displays sinusoidal REE patterns with peculiar and unexpected heavy REE (HREE) enrichments (e.g. Marks et al. 2004; Reguir et al. 2012). The fractionation of such HREE-rich Cpx from their parental magma may lead to the formation of HREE-rich cumulates with economic concentrations (Möller and Williams-Jones 2016). Such HREE enrichments of Cpx have been tentatively attributed to the preferential incorporation of HREE in the VI-coordinated M1 site, whereas light and middle REE (LREE and MREE, respectively) are preferentially incorporated in the VIII-coordinated M2 site (Bottazi et al. 1999; Fedele et al. 2009; Olin and Wolff 2010; Reguir et al. 2012, Beard et al. 2019). Cpx enriched in HREE relative to MREE also display uncommon positive Zr and Hf anomalies (e.g., Bakti et al. 2018; Baudouin et al. 2016; Marks et al. 2004; Weidendorfer et al. 2016). These substitutional variations seem to occur for specific compositions (e.g., high Mn or Na contents, usually in alkaline rocks), though HREE enrichments have been observed in both aegirine ($NaFe^{3+}Si_2O_6$) and diopside ($CaMgSi_2O_6$) (Marks et al. 2004; Möller and Williams-Jones 2016; Reguir et al. 2012; Weidendorfer et al. 2016; Beard et al. 2019). Subtle HREE

enrichments are also occasionally observed in basanite (Woodland and Jugo 2007) and in silica-saturated rocks such as diorites (e.g., Zhang et al. 2017). Sinusoidal patterns of REE partition coefficients are nevertheless not always observed for alkaline compositions. REE partitioning between diopside and trachy-phonolite melt suggests that all REE are substituted in the M2 site and no anomalous HREE distributions are observed (Mollo et al. 2016). Thus, Cpx, enriched or not in HREE, can equilibrate with phonolitic compositions, implying that the HREE-enrichments observed in some alkaline rocks may be dominated by the crystal-chemical framework of Cpx rather by the melt composition.

In the present study, we address the partitioning of trace elements between Cpx and silicate melt in alkaline systems, and the origin of HREE enrichments in Cpx from some alkaline igneous complexes. We determined the trace element partition coefficients for Cpx phenocrysts in equilibrium with phonolitic melt inclusions in ijolite cognate cumulates from Oldoinyo Lengai that document the active magma chamber, in which HREE-rich Cpx have previously been described (Mollex 2017). Based on our observed partition coefficient, we use the lattice strain model to improve our understanding of the substitution parameters of trace elements in the Cpx crystal sites (Blundy and Wood 1994). These new data are used alongside *D* values from literature to elaborate general equations based on Cpx chemistry that provide $D_i^{\mathrm{Cpx/melt}}$ for REE and high field strength elements (HFSE; Ti, Hf, Zr, Nb, Ta) in alkaline magmas.

Sample and Methods

Sample description

Oldoinyo Lengai is an active volcano that erupts both natrocarbonatite and alkaline silicate magmas (Dawson 1998; Keller and Krafft 1990; Mollex et al. 2018). During the sub-Plinian 2007–2008 eruption, various xenoliths including ijolite cognate cumulates were brought to the surface, providing samples from the active magma reservoir (Mollex et al. 2018). This eruption was triggered by the recharge of the magmatic reservoir, and the ijolite samples provide constraints from the mid-crustal reservoir (~13 km, 1000°C; de Moor et al. 2013; Baudouin and France 2019). We studied Cpx and Cpx-hosted melt inclusions in 3 ijolites (10TL01, 10TL05, 10TL06; Fig. A1), collected on the southern slope of the northern active crater. We focus our study on sample 10TL01 which contains the largest melt

inclusions (Fig. 1). The volatile element content, liquid line of descent, crystallization sequence, and origin of the sample were presented in detail by Mollex (2017).

Ijolite sample 10TL01 contains large crystals of Cpx, Ti-garnet (melanite), nepheline, apatite and minor sulfides, titanomagnetite, wollastonite, and interstitial glass. A single population of Cpx phenocrysts (100-1000 μm) is present in the studied sample, it displays a slightly patchy zoning with a restricted compositional variation (Fig. A1). Melt inclusions in Cpx are relatively small (≤50 μm), and their hosting Cpx show local chemistry variation (Fig. 1d). To minimize the effect of the local chemistry variation, Cpx-melt couples were analyzed very close to each other; melt-Cpx composition covariations will help us quantifying the dependence on composition of partition coefficients. ~10 % of the Cpx-hosted melt inclusions also contain small amount of carbonatite globule (<2% vol. of the whole melt inclusion volume), those inclusions have not been considered to estimate silicate melt - Cpx partitioning. Detailed petrographic observations have also shown that some melt inclusions contains daughter mineral (e.g., magnetite), and have therefore also not been considered to quantify melt - Cpx partitioning. Among the selected melt inclusions (n=16), Cpx have homogeneous composition around the melt inclusions, except for 1 Cpx-melt couple which displays a lighter shade in the BSE image (Fig.1c, cpx n°1 on table S1).

Major and trace element measurements

Major element concentrations in Cpx and glasses were determined using a CAMECA SX-100 electron microprobe at the Laboratoire Magmas et Volcans (LMV, Clermont-Ferrand, France). Analyses were performed using a 15 kV accelerating voltage. Minerals were analyzed using a focused beam and a 6 nA current, whereas melt inclusion measurements were performed using a spot size of 5 μm and a 4 nA current to prevent host mineral contamination and minimize alkali loss and beam damage of the glasses (errors in supplementary material).

Trace element concentrations were determined using a Thermo Element XR laser ablation inductively coupled plasma mass spectrometer at LMV. Laser beam diameters of 25 and 9 to 15 μm were used for Cpx and melt inclusions, respectively, with a laser repetition rate of 1–2 Hz and laser power of 4.8 $J \cdot cm^{-2}$ (laser excimer 193 nm Resonetics M-50E). Trace element concentrations were calibrated by using similar laser beam diameters, and international standard glasses NIST612 as primary standard, and NIST610 and BCR-2 as secondary standards; the SiO_2 and CaO concentrations previously determined by electron

158 microprobe for individual Cpx and glasses were used as internal standards (errors and
159 standards in supplementary material). The Glitter Software (Griffin et al. 2008) was used to
160 process the raw data files of signal intensity versus time.
161

162 # Results

163 ## Clinopyroxene chemistry
164

165 Cpx from Oldoinyo Lengai ijolites occur as large crystals (100–1000 µm) with
166 diopside to augite compositions ($Wo_{48}En_{38}Fs_{14}$ to $Wo_{44}En_{27}Fs_{29}$), and relatively low aegirine
167 components (Ae_6 to Ae_{21}) (Fig. 2). Cpx Mg# (= 100 × Mg/(Mg+Fe) in molar proportions)
168 range from 49 to 74 with relatively high Fe content (8.2–16.0 wt% FeO_t). Minor element
169 contents are 0.4–0.7 wt% Al_2O_3, 0.3–0.46 wt% TiO_2, 0.25–0.49 wt% MnO, and 1.0–2.5 wt%
170 Na_2O (Fig. 3a, Table S1). Fe^{3+} contents calculated using the stoichiometric method (Droop,
171 1987) are slightly lower than Fe^{2+} contents (Fe^{3+} = 0.05–0.22 per formula unit, p.f.u., vs. Fe^{2+}
172 = 0.14–0.36 p.f.u.; Fig. 3b). The T site is occupied by silicon with minor Al^{IV} (0.01–0.03) and
173 Fe^{3+} (0–0.03), the M1 site incorporates Fe^{3+}, Fe^{2+}, Mg^{2+}, Ti^{4+}, and Mn^{2+} cations, and the M2
174 site is filled by $Ca^{2+} + Na^{+}$ (= 1 p.f.u.).
175 Cpx REE contents, when normalized to chondrite, are characterized by a sinusoidal
176 pattern with a strong HREE enrichment. Cpx have low REE contents (e.g., 0.67–1.65 ppm La;
177 corresponding to 2–8 times chondritic values) and are enriched in LREE and HREE compared
178 to MREE ($(La/Dy)_N$ = 2.6–5.4 and $(Lu/Ho)_N$ = 6.2–8.8, where the subscript 'N' denotes
179 chondrite-normalized values, McDonough and Sun (1995) (Figs. 4a, A2). Cpx have high
180 incompatible element concentrations, with Sr varying from 547 to 720 ppm, Zr from 174 to
181 354 ppm, and low concentrations of Sc (2.7–4.3 ppm) and Nb (0.1–0.3 ppm) (Table S2). Cpx
182 have a distinct positive Zr-Hf anomaly relative to the primitive mantle, as evidenced by
183 $(Hf/Sm)_N$ ratios of 16.4–27.7 (Figs. 4b, A2 & A3).
184

185 ## Phonolite melt inclusions
186

187 Cpx-hosted melt inclusions have phonolitic compositions with SiO_2 contents varying
188 from 47.3 to 50.4 wt%, alkali ($Na_2O + K_2O$) from 17.8 to 21.9 wt% (Fig. 5, Table S1), and
189 very low MgO contents ranging from 0.03 to 0.38 wt%. CaO content varies from 0.54 to 2.09
190 wt%, FeO_t from 5.2 to 9.6 wt%, and Al_2O_3 from 10.9 to 17.7 wt% (Table S1). Melt inclusions
191 have high REE contents, with La varying from 40 to 210 ppm (200–1000 times chondritic

values, McDonough and Sun 1995), and are enriched in LREE compared to HREE with La/Yb varying from 8 to 38. Melt inclusions have high incompatible element concentrations with Sr contents ranging from 650 to 3730 ppm, Nb from 420 to 850 ppm, and Zr from 700 to 3180 ppm (Table S2, Fig. A2; A3).

Trace element partitioning

Cpx/phonolite melt trace element partition coefficients have been calculated from the concentrations measured in 16 Cpx-hosted melt inclusions and their Cpx hosts. However, melt inclusion compositions may be affected by post-entrapment crystallization, modifying the Cpx-melt equilibrium. If extensive, post-entrapment crystallization could result in the under- or over-estimation of partition coefficients for incompatible and compatible elements, respectively. The contribution of post-entrapment crystallization in the studied melt inclusions has been estimated to be ~9% based on experimentally determined Fe-Mg partition coefficients and DiHd composition parameter (Masotta et al. 2013; Mollo et al. 2013; details in supplementary material). For incompatible elements, post-entrapment crystallization of a few percent Cpx at melt inclusion margins does not modify the melt composition by more than few percent for incompatible elements (see calculation in supplementary material; Fig. A4). Taking in account both Analytical errors and post-entrapment crystallization, we estimate that our reported partition coefficients are accurate to within 10% (analytical errors in supplementary material).

Compared to literature data associated with basalts or phonolites (Adam and Green 2006; Hill et al. 2000; Mollo et al. 2016), the REE partition coefficients between Cpx and phonolite melt obtained herein 1) are significantly lower, 2) increase from LREE to MREE (D_{La} = 0.013 ± 0.005 and D_{Sm} = 0.062 ± 0.018, respectively), and from MREE to HREE (D_{Ho} = 0.062 ± 0.021 and D_{Lu} = 0.41 ± 0.14, respectively) (Fig. 6; Tables 1, S3), and 3) D_{HREE} such as D_{Lu} is not correlated with D_{LREE} (e.g., D_{La}), but displays a slight correlation with other trivalent cation partition coefficients like with D_{Sc} (Tables 1, S3).

The low LREE and MREE partition coefficients observed for alkaline magmas herein and in previous studies (Adam and Green 2006; Dalou et al. 2012; Hill et al. 2000; Mollo et al. 2016; Fig. 6) imply a strong REE enrichment of the residual liquid during Cpx crystallization. These uncommon partition coefficients associated with alkaline systems

therefore result in very high REE contents in the associated evolved melts (e.g., trachy-phonolite, phonolite, carbonatite).

Tetravalent HFSE have D values close to D_{HREE} (e.g., D_{Zr} = 0.13 ± 0.06 and D_{Hf} = 0.25 ± 0.1), similar to those observed for trachy-phonolite melt (Mollo et al., 2016) (Fig. 6, Table 1). Pentavalent HFSE have very low D values (e.g., D_{Nb} < 0.0005 and D_{Ta} < 0.003). Zr and Hf have higher partition coefficients than MREE, as highlighted by high D_{Hf}/D_{Nd} ratios (2–5.6; Fig. 7). Other Cpx trace element partition coefficients are as follows: D_{Sr} = 0.66 ± 0.23, D_{Ba} = 0.0002 ± 0.00006, D_{Th} = 0.0003 ± 0.0001, and D_V = 0.63 ± 0.33 (Table 1). In this study, we observe that Sr is only moderately incompatible and has a high partition coefficient relative to REE (Fig. A2), whereas Sr behaves more incompatibly in basaltic melts (Fig. 6).

Discussion

Lattice strain model parameters

Partition coefficients D_i can be modeled using lattice strain theory (Blundy and Wood, 1994) as:

$$D_i = D_0 \exp\left[\frac{-4\pi E N_A\left[\frac{r_0}{2}(r_i-r_0)^2+\frac{1}{3}(r_i-r_0)^3\right]}{RT}\right] \quad (1)$$

where D_i is a function of the cation radius (r_i), the partition coefficient (D_0) of the ideal cation with a radius r_0 (Å) for the crystallographic lattice M1 or M2, and an elastic constant E (Young's modulus, in GPa), as well as Avogadro's constant N_A (6.022×10^{23} mol^{-1}), the universal gas constant R (8.3145 J·mol^{-1}·K^{-1}), and temperature T (Kelvin). In Cpx, the six-fold coordinated M1 site incorporates tetravalent (Ti^{4+}, Zr^{4+}, Hf^{4+}) and trivalent cations (e.g., Cr^{3+}, Sc^{3+}) whereas the eight-fold coordinated M2 site preferentially incorporates REE^{3+} (e.g., Adam and Green 2006; Blundy and Wood 1994, 2003; Dalou et al. 2012; Hill et al. 2000). Detailed calculation of the strain energy in the lattice strain model (LSM) is provided in the supplementary material.

Trace element partitioning between Cpx and melt ($D_i^{\mathrm{Cpx/melt}}$) has been characterized and quantified by applying the LSM (Onuma et al. 1968) to various Cpx and melt compositions (e.g., Blundy et al. 1998; Gaetani and Grove 1995; Wood and Blundy 1997, 2001). In order to determine the effects of melt composition, Cpx chemistry, pressure, and temperature on partition coefficients, we compared our D values measured from Oldoinyo Lengai ijolite to a dataset including Cpx in equilibrium with phonolite (Mollo et al. 2016;

Olin and Wolff 2010), basalt (e.g., Dalou et al. 2012; Hill et al. 2000), and basanite melts (Adam and Green 2006). The LSM was applied to those *D* values using the SIMPLE FIT and DOUBLE FIT program (Dalou et al. 2018), which calculates the best-fit values of the lattice strain parameters (r_0, D_0, and E) for both clinopyroxene M-sites. DOUBLE FIT does not require assignments of elements per site or constraints on the LSM parameters to calculate the best-fit values and LSM parameters. However, we considered $HREE^{3+}$ as being either 6- or 8-fold coordinated (i.e., in the M1 or M2 site in Cpx, respectively) when fitting the REE data (see section 5.1.1). To obtain reliable estimates of r_0, D_0, and E, DOUBLE FIT requires a minimum of six D_i values: we therefore focused our study on the partitioning of trivalent (REE^{3+}, Cr^{3+}, Sc^{3+}). For tetravalent cations (Ti^{4+}, Zr^{4+}, Hf^{4+}), we use SIMPLE FIT (minimum of 3 D_i values) to determine M1 LSM parameters.

REE and trivalent cations

Previous studies have successfully applied the LSM to Cpx-melt partitioning, and the distribution of REE can be modeled by assuming that all REE are substituted for Ca in the M2 site (e.g., Hill et al. 2000; Mollo et al. 2016; Wood and Blundy 1997). Between Mg-rich Cpx and basaltic liquid, LREE are highly incompatible ($D_{La} \leq 0.1$), and incompatibility decreases toward the MREE with relatively constant *D* values between Ho and Lu (e.g., Wood and Blundy 2007; Hill et al. 2000; Wood and Blundy 1998) (Fig. 8). In contrast, the $D_{\mathrm{REE}}^{\mathrm{Cpx/phonolite}}$ values obtained herein are not consistent with the existing models (e.g. Blundy and Wood 1994); assuming incorporation of all REE in the M2 site: indeed HREE (Er to Lu) do not follow a parabolic repartition commonly explained by the LSM (Fig. 8), implying the substitution of HREE in both the M2 and M1 sites. It is therefore necessary to estimate D_0, r_0, and E for trivalent cations in both the M1 ($HREE^{3+}$, Sc^{3+}, Cr^{3+}) and M2 sites ($HREE^{3+}$, $MREE^{3+}$, $LREE^{3+}$, Fig. 8), which provides lattice strain parameters that differ significantly from the literature data (Bédard 2014; Dygert et al. 2014, Fedele et al. 2009; Olin and Wolff 2010). HREE incorporation in M1 have been previously suggested, but predictive model for D_{HREE} must be carefully determined yet.

Cpx-phonolite melt ${D_0}^{3+}$ parameters for the M2 site are very low (${D_0}^{3+} = 0.07 \pm 0.015$) relative to those obtained by Mollo et al. (2016); (${D_0}^{3+} = 1.07 \pm 0.27$; Table S4). Previous studies have shown the strong influence of Cpx Al^{IV} content on the ${D_0}^{3+}$ value of the M2 site (e.g., Hill et al. 2000; Mollo et al. 2016; Wood and Blundy 1997). The very low ${D_0}^{3+}$ value

obtained herein can thus be related to the very low Al^{IV} content of Oldoinyo Lengai Cpx (≤0.03 p.f.u., Table S1). The LSM parameters obtained herein are also characterized by relatively high r_0^{M2} (i.e., 1.05 Å), and E^{M2} values within the range of previous studies related to low pressure (E = 325–441 GPa; Hill et al., 2000; Mollo et al. 2016; Tables 2, S4, S5).

The LSM parameters for the M1 site are D_0^{3+} = 1.24 ± 0.44, E^{3+} = 382 ± 48 GPa, and r_0^{3+} = 0.74 ± 0.006 Å (Table 2, Fig. 9). D_0^{3+} and E are inter-correlated and display very low values compared to other studies of basaltic to phonolitic compositions (Dalou et al. 2012; Hill et al. 2000; Olin and Wolff 2010). The ideal cation radii (r_0) are among the largest reported, except those for HREE-bearing M1 sites from Olin and Wolff (2010) (r_0^{M1} = 0.72–0.77 Å). HREE incorporation in the M1 site thus seems to be promoted by high r_0^{3+} (>0.7 Å) and low E^{3+} (<500 GPa) of this crystallographic site (Figs. A5, A6, A7).

HFSE

HFSE (4+ and 5+ cations) are commonly considered to be incorporated in the M1 site (i.e., six-fold coordination; e.g., Wood and Blundy 2007). By studying their partitioning behavior, we obtain information on the properties of the M1 site, and on their dependence on Cpx chemistry (Figs. 10 A6). Due to the very low partition coefficients for Nb and Ta (e.g., D_{Nb} = 0.0001–0.0005) and uncertainties on the valence of vanadium (3+, 5+; Adam and Green, 2006), we applied the LSM only for tetravalent (Ti^{4+}, Zr^{4+}, Hf^{4+}) and not pentavalent HFSE. Obtained LSM parameters are D_0^{4+} = 0.73–1.08, E^{4+} = 1736–2397 GPa, and r_0^{4+} = 0.655–0.662 Å (Table 2, Fig. A8). The r_0^{4+} of the M1 site correlates with Cpx chemistry (Fig. A8) but is particularly large when compared to values of previous studies (e.g., Blundy et al. 1997; Hill et al. 2000; Mollo et al. 2016; 2018), particularly. The D_0 and E values obtained herein are lower than those for Mg-Al rich Cpx (Hill et al. 2000; Table S5) and similar to those of Fe-rich Cpx (Dygert et al. 2014).

Factors controlling trace element partitioning in Cpx

The specific features of Cpx trace element compositions, and of the associated partition coefficient distribution determined herein (e.g., HREE and Zr-Hf enrichments relative to MREE in Cpx, as well as their covariation highlighted by a well-defined $(Zr/Nd)_n$ vs $(Lu/Ho)_N$ correlation; Fig. 7a) are observed in several other alkaline complexes (Figs. 4, 7a). In this study, these anomalies are associated with higher D_{Zr}/D_{Nd} and D_{Lu}/D_{Ho} ratios

compared to the literature (D_{Zr}/D_{Nd} and D_{Lu}/D_{Ho} < 1.2, Fig. 7b; Adam and Green 2006; Hill et al. 2011; Mollo et al. 2016).

The partitioning of trace elements between Cpx and melt varies with intensive parameters (pressure, temperature, redox conditions), melt composition, and Cpx chemistry (e.g., Bennett et al. 2004; Blundy et al. 1998; Hill et al. 2011; Olin and Wolff 2010).

Pressure and temperature are expected to have a strong effect on ideal cation radius (r_0) and partition coefficients (e.g., Hill et al. 2011). However, Cpx-melt partition coefficients acquired over a large pressure and temperature range do not display an effect on HREE partitioning in the M1 site for basalts (Adam and Green 2006; Dalou et al. 2012; Hill et al. 2000) or even trachy-phonolite melt equilibrated in the same pressure range as our study (≤350 MPa; Mollo et al. 2016). The low equilibrium D_0^{M2}values determined herein at low pressure and moderate temperature conditions (~300 MPa and 1050 °C) should therefore be attributed to other parameters.

Melt composition (e.g., silica, alkali, or volatile contents) influences the melt structure, and trace element partition coefficients usually decrease with increasing melt polymerization (characterized by the number of non-bridging oxygens per tetrahedral cation, NBO/T; Gaetani 2004; Huang et al. 2006, Michely et al. 2017, Mollo et al., 2016; Figs. A9 & A10). According to those studies, an increasing in NBO/T value would imply an important decrease of the partition coefficients down to one order of magnitude (when NBO/T rises from 0.2 to 2). However, There is no correlation between NBO/T and HREE enrichment for phonolite and basalt melts (e.g., NBO/T = 0.61–0.8 at D_{Lu}/D_{Er} > 5 for phonolite and NBO/T = 0.5–0.7 at D_{Lu}/D_{Er} = 0.93–1.17 for basalts; Gaetani, 2004). In the case of $D_{HREE} > D_{MREE}$ (Beard et al. 2019; Olin and Wolff 2010, this study), the melt polymerization and composition effect on partition coefficient seems to be negligible in comparison to the effect of mineral chemistry (Figs. A10). Michely et al. (2017) observe correlations between melt Na_2O content and trace element partition coefficients. The influence of Na over trace element partitioning may apply only in the case of Na-poor melts (0-2.5 wt% Na_2O), since we do not observe any relationship between Na_2O or K_2O content in our melts (varying between 6 and 13 wt%) and trace element partition coefficients (Fig. A10).

HREE enrichment in Cpx is therefore not related to specific pressure conditions or melt composition (basalt/phonolite), but can likely be related to the Cpx chemistry. Partition coefficient values have been shown to rise with increasing Al^{IV} content (Gaetani and Grove 1995, and Lundstrom et al. 1994, Wood and Blundy 1997). In addition, HREE enrichment in Mn-rich Cpx (MnO = 2.4–2.9 wt%) negatively correlates with Fe^{2+} and positively

359 correlates with Mn^{2+} content (Olin and Wolff 2010). Cpx Na content may also exert a
360 dominant control on REE partitioning following the substitution $Na^{+} + REE^{3+} = 2\ Ca^{2+}$ (Wood
361 and Blundy 1997), although this correlation has only been observed for extremely Na-rich
362 Cpx (2.2–13.5 wt% Na_2O) at high-pressure conditions (>3 GPa; e.g., Bennett et al. 2004). The
363 role of Cpx chemistry, observed at high pressure, needs to be further investigated for Na-rich
364 clinopyroxenes crystallized at low pressure (see the discussion below).

365 Here we have used a $D^{Cpx/melt}$ dataset for melt compositions ranging from basalt to
366 phonolite, with and without HREE anomalies, to track the origin of the anomalous partition
367 coefficients observed in various alkaline complexes (Figs. 4–7; Adam and Green 2006; Dalou
368 et al. 2012; Hill et al. 2000; Mollo et al. 2016; Olin and Wolff 2010). LSM parameters are
369 correlated with high D_{HREE}/D_{MREE}: specifically, high r_0^{3+} values for the M1 site (0.73–0.75 Å)
370 are well correlated to Cpx chemistry (e.g. Mg/Fe and Na/Ca ratios) and to the HREE
371 enrichment (Fig. 9, A6, A7), that can be quantified by the parameter Lu* (see section 5.3.1 for
372 further details):

373 $$\text{Lu*}\ (\%) = [D_{Lu}^{M1} / (D_{Lu}^{M1} + D_{Lu}^{M2})] \times 100 \quad (2)$$

374 In the M1 site, r_0^{3+} increases along with Fe^{3+} content and decreases with Mg^{2+} and
375 Al^{IV} contents increase (Fig. 9, Table S5), whereas E^{3+} is negatively correlated with r_0^{3+} and
376 increases along with Mg content (Fig. A7). Cameron and Papike (1980) showed that the
377 nature and size of the main cation in the M2 site has an influence on the ionic radius of the
378 M1 site. In the present study, the ionic radius of the M1 site is sensitive to Mg/Fe and
379 Fe^{3+}/Fe^{2+} ratios. In the absence of Al (i.e., the jadeite pole), Na^{+} atoms are charge balanced
380 with Fe^{3+} (i.e., the aegirine pole) as observed herein and at various alkaline complexes (Fig.
381 2). As r_0^{3+} in the M1 site is strongly dependent on Mg and Fe^{3+} content and well correlated
382 with HREE enrichment (high Lu*; Fig. 9), aegirine and Mg contents seem to be the main
383 chemistry factors inducing HREE incorporation in the M1 site. HREE enrichments should
384 therefore be prevalent in the presence of Fe^{3+} in Cpx (thus under oxidizing conditions), and in
385 alkaline magmatic systems that allow charge balance between trivalent (Fe^{3+}) and monovalent
386 (Na^{+}) cations instead of two bivalent cations ($Mg^{2+} + Ca^{2+}$; the diopside pole). Furthermore,
387 Cpx crystals may record magmatic differentiation with Fe-rich and more oxidized (Fe^{3+}-rich)
388 composition, leading to significant enrichment in HREE and high Hf/Sm ratios (Woodland
389 and Jugo 2007).

The observed high D_{HREE}/D_{MREE} are strongly correlated with high D_{Zr} and D_{Hf} values relative to MREE (e.g., D_{Hf}/D_{Sm} and $D_{Zr}/D_{Nd} > 2$; Figs. 6, 7). This is mostly due to the low D_{MREE} values, as the partition coefficients of Zr and Hf are within the range of literature data (Fig. 6). D_{Zr}/D_{Nd} increases with increased r_0^{4+} in the M1 site, which is related to increased Fe^{3+} content and decreased Al^{IV} and Mg contents (Fig. A8).

Parameterization of the trace element distribution

Prediction of HREE enrichment

In the following section, we propose a parameterization based on Cpx major element composition only that allows prediction of Cpx HREE enrichment (high D_{Lu}/D_{Ho}; Fig. 11), and associated partition coefficients. Neither trace element quantification, nor melt composition are required to proceed with D estimate. Parameterization constants along with the corresponding spreadsheet built to predict REE partitioning between clinopyroxene and alkaline evolved melts are provided in supplementary material, and described below. Data used for the parameterization are from this study, Adam and Green (2006); Dalou et al. (2012); Hill et al. (2000); Mollo et al. (2016) and Olin and Wolff (2010).

Parameters that may influence HREE enrichment (i.e., Lu*) such as pressure, temperature, and composition were tested using a multiple linear regression (Excel Analysis "ToolPak") to determine the main influencing variables. As Lu* is well correlated with r_0^{M1} and Cpx chemistry (Figs. 9, A6), we further quantify the observed HREE enrichment as a function of the main influencing cation contents (Mg, Ca, Fe, Al). The impact of each major element and estimated temperature on Lu* is best reproduced by the following equation:

$$Lu^* = a_{Lu}\,T + b_{Lu}\,Fe^{3+} + c_{Lu}\,Al^{VI} + d_{Lu}\,Mg + e_{Lu}\,Ca + g_{Lu} \qquad (r^2 = 0.84), \qquad (3)$$

where element contents are expressed in formula units (calculated with 6 oxygen atoms), temperature in °C, and the fit parameters are $a_{Lu} = 0.098$, $b_{Lu} = 175$, $c_{Lu} = -222.07$, $d_{Lu} = -97.81$, $e_{Lu} = 57.59$, $g_{Lu} = -41.73$ (Table S6). This parameterization is calibrated over a range of Cpx compositions (expressed in moles p.f.u., Fe^{3+} = 0-0.3, Al^{VI} = 0-0.3, Mg = 0.2-0.9, Ca = 0.5-1), and temperatures (700-1400°C). Equations similar to equation (3) are obtained for the other HREE (Er*, Tm*, and Yb*) with the parameters provided in Table S6.

The equation (3) and fit parameters presented in Table S6 highlight the significant role of Fe^{3+} and Mg, and to a lesser extent those of temperature, Al^{VI}, and Ca, in influencing HREE partitioning in Cpx. As the Lu*, Er*, Tm*, and Yb* parameters are based mainly on the Cpx major element composition, they can be calculated to predict anomalous HREE enrichment for any Cpx crystal. The reliability of our parameterization was tested using $(Lu/Ho)_N$ ratios in Cpx from various alkaline provinces worldwide; alkaline syenites, Bakti et al. 2018; Marks et al. 2004; Möller and Williams-Jones 2016; Vuorinen et al. 2005; nephelinites, Baudouin et al. 2016; Weidendorfer et al. 2016; and phonolites, Baudouin and Parat 2015). This independent set of data show a very good correlation between the Lu* parameter calculated with equation (3) based on major elements only, and the observed HREE enrichment expressed by the ratio $(Lu/Ho)_N$ of natural Cpx (Fig. 12 (r^2 =0.8).

Prediction of REE element partitioning

By quantifying the Lu*, Er*, Tm*, and Yb* parameters, we can then determine anomalous *D* values for those elements from Cpx major element compositions, P, T and $Mg\#^{melt}$. HREE* and LSM parameters on M2 can be used to quantify D_{REE} without using LSM parameters of the M1 site, when data available from literature to apply a well constrain multiple regression are too rare.

Mollo et al. (2016) adapted the LSM equations proposed by Wood and Blundy (1997) for REE partitioning between Cpx and trachy-phonolite magmas. Their model quantifies REE^{3+} partitioning between melt and the M2 site of Cpx: D_0* is obtained from pressure, *T*, $Mg\#^{melt}$, and X_{Mg}^{cpx}, when r_0* and *E** are calculated from X_{Ca}^{cpx} and X_{Mg}^{cpx} (where $X_{Mg,Ca}^{cpx}$ represents the mole fraction of each element in Cpx; Fig. A11). We applied equations from Wood and Blundy (1997), Mollo et al. (2016) and Beard et al. 2019 to our Cpx-melt pairs (Fig. 13). Wood and Blundy (1997) and Mollo et al. (2016) successfully reproduce the measured LREE and MREE partition coefficients (from La to Ho), but significantly underestimate those of HREE (Er, Tm, Yb, Lu). Beard et al. (2019) model strongly overestimate all REE partition coefficients and only reproduce correctly D_{Lu} (Figs. 13, A11). Beard et al. (2019) model manages to predict D_{REE} within 1 order of magnitude of confidence for most of basaltic to phonolitic melt compositions (with pressure, temperature and Cpx major element composition as input parameters; Fig. A12). Nevertheless we believe that one order of magnitude of confidence is too large when considering partition coefficients and

related igneous petrology models. Beard et al. (2019) models display important discrepancy between measured and predicted partition coefficients at a smaller scale (Fig. A12). In order to improve those previous calibrations we present hereafter a new model to account for the identified discrepancies.

The partition coefficient of Lu can be modeled as a function of the Lu* parameter, D_0* and E* (M2 site) as:

$$D_{Lu} = h_{Lu}\,Lu^* + j_{Lu}\,D_0^* + k_{Lu}\,E^* + l_{Lu}. \quad (4)$$

where h_{Lu} = 0.008, j_{Lu} = 0.76, k_{Lu} = -0.0018, and l_{Lu} = 0.62. Equations similar to equation (4) can be obtained for Er*, Tm*, and Yb* by using the fit parameters presented in the Table S6. D_0* and E* are obtained using equations (5)-(6)-(7) presented below.

The partition coefficients estimated using equation (4) are relevant when Lu* (or Er*, Tm*, Yb*) > 40% (HREE incorporated in both sites). Fig. 13 highlights the improvement of this approach in determining D_{HREE} when Lu* > 40%. When HREE enrichment is low (i.e. Lu*<40%), we recommend to calculate D_{HREE} from Mollo et al. (2016) approach, that was calibrated for phonolitic and trachy-phonolitic melts (spreadsheet for details).

In equation (4), D_0* and E* for trivalent cations (M2 site) are obtained by using equation (5) and (6) (Wood and Blundy 1997; Mollo et al. 2016):

$$D_0^* = \frac{Mg\#_{melt}}{XMg^{M1}} * \exp\left(\frac{88750 - 65.644*T + 7050P - 770P^2}{RT}\right) \quad (5)$$

$$E^* = -82.35 + 636.56 * X_{Ca}^{cpx} - 253.29 * X_{Mg}^{cpx} \quad \text{(GPa)} \quad (6)$$

However, those equations require knowledge of the melt composition to obtain D_0* and thus D_{REE}. In order to facilitate the use of our new model, we propose that for phonolite and trachyte compositions and for a range of temperature from 840 to 1020°C, D_0* can be expressed as a function of Al_{Cpx}^{IV} only (for Al_{Cpx}^{IV} <0.15 p.f.u.), facilitating the use of the proposed parametrization (Fig. A13) as:

$$D_0^* = 10.434 \times Al_{Cpx}^{IV} + 0.0384. \quad (r^2 = 0.93) \quad (7)$$

D_0* calculated from Al^{IV}_{Cpx} is relevant for a smaller range of Cpx composition than equation (5), however Cpx with low Al^{IV} content (Al^{IV}_{Cpx} <0.15 p.f.u) is common in alkaline rocks (syenite, phonolite, alkali-rich nephelinite, Fig 3b). Furthermore, Cpx with low Al content and moderate aegirine content are often related to alkaline igneous complexes associated with carbonatites (Marks et al. 2004, Weidendorfer et al. 2016, Vuorinen et al. 2005). Finally the parametrization of REE partition coefficients between alkaline melt and Cpx that is proposed herein allows one to obtain D_{REE} from major element composition of Cpx only, T should also be estimate (spreadsheet available in supplementary table).

Determination of HFSE partition coefficients

The parameterization of HFSE partition coefficients can also be improved for the phonolite and trachy-phonolite alkaline magmas studied herein and in Mollo et al. (2016). We revisited the covariations between D_{Ta} and Al^{IV}, D_{Hf} and D_{Zr}, D_{Ti} and D_{Zr}, and D_{Ti} and Al^{IV} previously identified by Wood and Blundy (2007) in Fig. 10 by using the new partitioning data presented herein and data from Mollo et al. (2016)(spreadsheet available in supplementary table). The corresponding new equations valid for alkaline magmas are:

$$D_{Ta} = 2.1976 \times (Al^{IV})^{1.9828}, \quad (r^2 = 0.83) \quad (8)$$

$$D_{Ti} = 12.231 \times Al^{IV} + 0.1228. \quad (r^2 = 0.79) \quad (9)$$

$$D_{Zr} = (D_{Ti} + 0.1268) / 5.905 \quad (r^2 = 0.69) \quad (10)$$

$$D_{Hf} = 1.0823 \times D_{Zr} + 0.2015, \quad (r^2 = 0.95) \quad (11)$$

Implications for REE evolution in alkaline magmatic systems

Trace element contents of melts strongly increase during protracted fractional crystallisation from mafic to highly alkaline magmas (i.e. phonolite), leading to the formation of the critical metal deposits (e.g., Nb, REE) that are associated with carbonatites and silicate alkali-rich magmas (e.g., Mountain Pass, USA; Ilmaussaq, Greenland). The budget of REE and HFSE in evolved melts strongly depends on the crystallized phase assemblage, and on their related partition coefficients. Cpx is a common mineral in alkaline magmas, and thus has

a major impact on their liquid line of descent, and on the one of associated carbonatites. The new partition coefficients presented herein highlight that HREE-rich Cpx likely form with the potential to promote LREE/HREE fractionation during magmatic differentiation. LREE-rich residual evolved melts, and associated high HREE/MREE Cpx cumulates can thus be produced (Fig. 14). Differentiation of phonolite melts may thus lead to evolved melts with similar HREE contents than that of mined carbonatites and thus clearly represent potential economic interests (Fig. 14). Cpx is not the only phase to crystallise from alkaline evolved magmas, and additional minerals such as nepheline, mica, sodalite, feldspar must be considered to quantify properly REE evolution in alkaline systems (e.g., Braunger et al. 2018, Marks et al. 2004, Vuorinen et al. 2005,). Crystallization of accessory minerals such as wollastonite, apatite, titanite may also have a huge impact on REE distribution between melts and cumulates Fig. 14).

Conclusions

Our study highlights the low LREE and MREE partition coefficients and relative HREE enrichment of Cpx crystallized from alkaline melts (phonolite). We have characterized REE partitioning between Cpx and melt by applying the lattice strain model. HREE enrichments are well correlated with the ideal ionic radius for trivalent cations r_0^{3+} in the M1 site, which is strongly dependent on Cpx chemistry: r_0^{3+} increases with increasing Fe^{3+} content and decreases with increasing Mg^{2+} and Al^{VI} contents. This dependence of HREE partitioning on Cpx chemistry allowed us to quantify HREE enrichment as a function of the main influencing major element cation contents (Mg, Ca, Fe, Al) and temperature.

In our study, we proposed equations to predict HREE partitioning between Cpx and alkaline melts without trace element measurements or knowledge of the exact melt composition. Finally, we improved the parameterization of HFSE partition coefficients for phonolite and trachy-phonolite alkaline magmas. A spreadsheet designed to apply the various models presented herein is provided as supplementary material.

Those results suggest that when considering alkaline series, the likely large LREE/HREE fractionation that may develop during Cpx or wollastonite crystallization could eventually produce cumulates enriched in HREE, and residual melts enriched in LREE that can then evolve to alkali-rich silicate melts and/or carbonatitic magmas. Both “HREE-rich” cumulates, and LREE-rich melts may thus ultimately form economically viable REE deposits.

Acknowledgments

We thank C. Beard, P. Ulmer, D. Weidendorfer, and 2 anonymous reviewers for their useful comments. We also thank the Tanzania commission for science and technology (COSTECH) for the field permits. The authors acknowledge the help of Robert Dennen for English editing. This research was financially supported by the French National Research Agency through the national program “Investissements d'avenir” with the reference ANR-10-LABX-21 01/LABEX RESSOURCES21, and through the project GECO-REE (ANR-16-CE01-0003-01; P.I.: Lydéric France). This study has also been supported by the Région Lorraine, and Région Grand-Est, and PNP and CESSUR programs from INSU-CNRS (grants to Lydéric France). This is CRPG contribution n° XX, and GECO-REE contribution n°XX.

Figure captions

Fig. 1. (a) Photomicrograph of clinopyroxenes hosted melt inclusions (reflected light) and (b) (c) (d) BSE images from Oldoinyo Lengai melt inclusions. For the image (d), a small "lighter" Cpx area is present which correspond to small chemical variation (dashed line). The melt inclusions are likely CO_2-rich (deMoor et al. 2013) accounting for the large shrinkage bubbles that are present; those presently containing residual polishing material. Major and trace elements analyses of Cpx have been performed close to the melt inclusions. Numbers correspond to the analyses reported in Table S1 & S2. Scale bars correspond to 10 µm.

Fig. 2. (a) Wollastonite (Wo)-Enstatite (En)-Ferrossilite (Fs) ternary diagram illustrating the chemical variability of clinopyroxenes from various alkaline complexes. (b) Classification of pyroxenes determined by Ca-Mg-Fe (Q = Wo-En-Fs), aegirine (Aeg) and jadeite (Jd) components. (c) expanded Q-Aeg-Jd diagram (b) with Q > 80% (Morimoto 1988). Clinopyroxene data are from Oldoinyo Lengai, Tanzania (this study, data used to calculate D), Hanang volcano, Tanzania (Baudouin et al. 2016), Cape Verde (Weidendorfer et al. 2016), Gronnedal-Ika, Greenland (Marks et al. 2004), Ditrău, Romania (Bakti et al. 2018) and from partition coefficient studies (natural samples: Mollo et al. 2016, Olin and Wolff 2010 and experimental studies: Beard et al. 2019, Hill et al. 2000, 2011; Dalou et al. 2012, Adam and Green 2006).

Fig. 3. Cpx mineral chemistry. (a) Na vs Mg and (b) Fe^{3+} vs Al^{IV}; p.f.u. = per formula unit, calculated for six oxygens. Fe^{3+} content of Cpx has been determined following the method of Droop (1987). Cpx data are from Oldoinyo Lengai (this study), Hanang volcano, Tanzania (Baudouin et al. 2016), Campi Flegrei, Italy, (Mollo et al., 2016), Ditrău, Romania (Bakti et al. 2018), Cape Verde (Weidendorfer et al., 2016), Tenerife (Olin and Wolff 2010), Gronnedal-Ika, Greenland (Marks et al. 2004) and experimental studies: Beard et al. 2019, Hill et al. 2000, 2011; Dalou et al. 2012, Adam and Green 2006).

Fig. 4. Trace element variation diagrams for clinopyroxenes. (a) REE concentrations normalized to chondrite and (b) extended trace element concentrations normalized to the primitive mantle for diopside (Oldoinyo Lengai, this study; Baudouin et al., 2016; Campi Flegrei, Mollo et al., 2016; Tenerife; Olin and Wolff 2010; Cape Verde; Weidendorfer et al.,

2016) and aegirine (Gronnedal-Ika, Marks et al., 2004). Normalization values are from McDonough and Sun (1995).

Fig. 5. Major element composition of Cpx-hosted melt inclusions studied herein (10TL01 ijolite sample, (a) alkali vs SiO_2, (b) FeO vs SiO_2, (c) K_2O vs SiO_2, and (d) CaO vs SiO_2. Melt composition from Beard et al. (2019), Mollo et al. (2016), Olin and Wolff (2010), Hill et al. (2000), Dalou et al. (2012) and Adam & Green (2006) are also reported for comparison.

Fig. 6. Trace element partition coefficients ($D^{Cpx/melt}$) obtained in this study (alkali-rich phonolite, Oldoinyo Lengai) and previous studies (experimental studies: Beard et al. 2019, Adam and Green, 2006; Dalou et al., 2012; Hill et al., 2000, 2011; and natural samples: Mollo et al., 2016; Olin and Wolff, 2010). Elements are ranked according to cation charge and increasing ionic radius.

Fig. 7. (a) Zr/Nd vs Lu/Ho ratios in Cpx normalized to the primitive mantle (n subscript). (b) Partition coefficient ratios between Zr and Nd *vs* Lu and Ho, highlighting the anomalous distribution of HREE and HFSE compared to MREE between Cpx and phonolite melts.

Fig. 8. Lattice Strain model best fit to Oldoinyo Lengai Cpx. Red circles represent measured $D^{Cpx/phonolite\ melt}$ values (error bars show 1σ uncertainties), and red and blue lines represent fits for the M1 and M2 sites. Ionic radii are from Shannon (1976). The fit to data from Hill et al. (2000) is also reported for comparison (open diamonds, dashed and dotted black lines represent the M1 and M2 site best fits).

Fig. 9. Effect of Cpx chemistry on the ideal ionic radii for trivalent cations (r_0^{3+}) in the M1 site: (a) Mg and (b) Fe^{3+} contents per formula unit (p.f.u.). Symbols color code represents the measured parameter Lu* (%) = $[D_{Lu}^{M1} / (D_{Lu}^{M1} + D_{Lu}^{M2})] \times 100$. Data presented here are from this study (Oldoinyo Lengai, with black circles), Adam and Green (2006); Baudouin and Parat (2015); Dalou et al. (2012); Hill et al. (2000); Mollo et al. (2016) and Olin and Wolff (2010).

Fig. 10. Parameters controlling HFSE partition coefficients: (a) D_{Ti} *vs* Al^{IV} (p.f.u.), (b) D_{Ti} *vs* D_{Zr}, (c) D_{Ta} *vs* Al^{IV}, and (d) D_{Hf} *vs* D_{Zr}. Open squares present data compiled in Wood and Blundy (2007) for basaltic melts. Red circles present data from this study, compiled in Table

S3 and green triangles are data from Mollo et al. (2016, Table S3) and diamonds are data from Beard et al. 2019 (light blue diamonds: experimental data; dark blue diamonds: Canary Islands data). Curves represent the best fits for phonolite melts in red (modeled from equations presented in the equations 8 to 11) and for basaltic melts in black (modeled from Wood and Blundy, 2007).

Fig. 11. Lattice strain model curves for DREE in six-fold (M1 site, red curve) and eight-fold (M2 site, blue curve) coordination, and the sum of the two curves (black curve). Red circles represent measured $D^{Cpx/phonolitic\ melt}$ values. DREE for each sites are calculated by using the equations described in the text section "Calculation of the strain energy (ΔG)".

Fig. 12. Lu/Ho ratio in Cpx normalized to the primitive mantle (n subscript) *vs* Lu* calculated from the major element content of Cpx (equation 3). No melt data are available for the Cpx presented here. The color scale shows the Fe^{3+} content in Cpx varying from 0 to 0.3 p.f.u. Cpx data are from Bakti et al. (2018), Baudouin and Parat (2015), Baudouin et al. (2016), Marks et al. (2004), Möller and Williams-Jones, (2016), Vuorinen et al. (2005), and Weidendorfer et al. (2016). Normalization values are from McDonough and Sun (1995).

Fig. 13. REE partition coefficients *vs* ionic radii. Measured partition coefficients (red circles) and those calculated in this study (OL= Oldoinyo Lengai sample, open circles) are in good agreement, especially for HREE (Er, Tm, Yb, Lu). Calculated partition coefficients from the lattice strain model using parameters derived from Beard et al. (2019, blue diamonds); Mollo et al. (2016, green triangles) and Wood and Blundy (1997, black diamonds) fail to reproduce the Cpx-alkaline melt HREE partition coefficients studied herein.

Fig. 14. REE evolution of phonolitic melt through fractional crystallization (%crystallization=85%). Evolved melt (full lines) and cumulates (dotted lines) are calculated by using partition coefficients calibrated for basalt (A. & G. 2006: Adam and Green 2006) and for phonolite (this study) to highlight the importance of using the accurate partition coefficient values if we are to quantify melt and cumulate REE contents. Presented models highlight that REE contents similar to natural carbonatites can be obtained (Bayan Obo carbonatites, Yang et al. 2000; Alnö carbonatites, Hornig-Kjarsgaard 1998). We also report crystallization model including 10% of wollastonite (partition coefficient from B. & F. 2019:

667 Baudouin and France 2019). Crystallization of accessory minerals such as wollastonite (as
668 well apatite, titanite) have a potential strong impact on REE distribution between melt and
669 cumulates and should thus be considered.
670
671
672
673

674 References
675

676 Adam J, Green T (2006) Trace element partitioning between mica-and amphibole-bearing
677 garnet lherzolite and hydrous basanitic melt: 1. Experimental results and the investigation
678 of controls on partitioning behaviour. Contrib. Mineral. Petrol. 152(1), 1-17.

679 Batki A, Pál-Molnár E, Jankovics MÉ, Kerr AC, Kiss B, Markl G, Heincz A, Harangi S
680 (2018) Insights into the evolution of an alkaline magmatic system: An in situ trace element
681 study of clinopyroxenes from the Ditrău Alkaline Massif, Romania. Lithos, 300, 51-71.
682 https://doi.org/10.1016/j.lithos.2017.11.029

683 Baudouin C, France L (2019) Trace element partitioning between wollastonite and alkaline
684 silicate magmas. Chemical Geology, 523, 88-94.

685 Baudouin C, Parat F (2015) Role of volatiles (S, Cl, H_2O) and silica activity on the
686 crystallization of haüyne and nosean in phonolitic magmas (Eifel, Germany and Saghro,
687 Morocco). American Mineralogist, 100(10), 2308-2322. https://doi.org/10.2138/am-2015-
688 5318

689 Baudouin C, Parat F, Denis CM, Mangasini F (2016) Nephelinite lavas at early stage of rift
690 initiation (Hanang volcano, North Tanzanian Divergence). Contrib. Mineral. Petrol.
691 171(7), 64. doi: 10.1007/s00410-016-1273-5

692 Beard, CD, van Hinsberg, VJ, Stix, J, Wilke, M (2019) Clinopyroxene/melt trace element
693 partitioning in sodic alkaline magmas. Journal of Petrology.

694 Bédard JH (2014) Parameterizations of calcic clinopyroxene—Melt trace element partition
695 coefficients. Geochemistry, Geophysics, Geosystems, 15(2), 303-336.

696 Bennett SL, Blundy J, Elliott T (2004) The effect of sodium and titanium on crystal-melt
697 partitioning of trace elements. Geochimica et Cosmochimica Acta, 68(10), 2335-2347.
698 https://doi.org/10.1016/j.gca.2003.11.006

699 Blundy J, Wood B (1994) Prediction of crystal–melt partition coefficients from elastic
700 moduli. Nature, 372(6505), 452.

701 Blundy J, Wood B (2003) Partitioning of trace elements between crystals and melts. Earth and
702 Planetary Science Letters, 210(3-4), 383-397. https://doi.org/10.1016/S0012-
703 821X(03)00129-8

704 Blundy JD, Robinson JAC, Wood BJ (1998) Heavy REE are compatible in clinopyroxene on
705 the spinel lherzolite solidus. Earth and Planetary Science Letters, 160(3), 493-504.
706 https://doi.org/10.1016/S0012-821X(98)00106-X

707 Bottazzi P, Tiepolo M, Vannucci R, Zanetti A, Brumm R, Foley SF, Oberti R (1999) Distinct
708 site preferences for heavy and light REE in amphibole and the prediction of Amph/L D
709 REE. Contrib. Mineral. Petrol. 137(1-2), 36-45.

710 Braunger, S., Marks, M. A. W., Walter, B. F., Neubauer, R., Reich, R., Wenzel, T., Markl, G.
711 (2018) The petrology of the Kaiserstuhl Volcanic Complex, SW Germany: the importance of
712 metasomatized and oxidized lithospheric mantle for carbonatite generation. Journal of
713 Petrology, 59(9), 1731-1762.
714

Brice JC (1975) Some thermodynamic aspects of the growth of strained crystals. Journal of Crystal Growth, 28(2), 249-253. https://doi.org/10.1016/0022-0248(75)90241-9

Cameron M, Papike JJ (1980) Crystal chemistry of silicate pyroxenes. Reviews in Mineralogy and Geochemistry, 7(1), 5-92.

Dalou C, Koga KT, Shimizu N, Boulon J, Devidal JL (2012) Experimental determination of F and Cl partitioning between lherzolite and basaltic melt. Contrib. Mineral. Petrol. 163(4), 591-609. doi: 10.1007/s00410-011-0688-2

Dalou C, Boulon J, Koga KT, Dalou R, Dennen R (2018). DOUBLE FIT: Optimization procedure applied to lattice strain model. Computers & Geosciences, 117, 49-56.

Dawson JB (1998) Peralkaline nephelinite–natrocarbonatite relationships at Oldoinyo Lengai, Tanzania. Journal of Petrology, 39(11-12), 2077-2094. https://doi.org/10.1093/petroj/39.11-12.2077

de Moor JM, Fischer TP, King PL, Botcharnikov RE, Hervig RL, Hilton DR, Ramirez C (2013). Volatile-rich silicate melts from Oldoinyo Lengai volcano (Tanzania): Implications for carbonatite genesis and eruptive behavior. Earth and Planetary Science Letters, 361, 379-390.

Droop GTR (1987). A general equation for estimating Fe^{3+} concentrations in ferromagnesian silicates and oxides from microprobe analyses, using stoichiometric criteria. Mineralogical magazine, 51(361), 431-435.

Dygert N, Liang Y, Sun C, Hess P (2014) An experimental study of trace element partitioning between augite and Fe-rich basalts. Geochimica et Cosmochimica Acta, 132, 170-186. https://doi.org/10.1016/j.gca.2014.01.042

Fedele L, Zanetti A, Morra V, Lustrino M, Melluso L, Vannucci R (2009) Clinopyroxene/liquid trace element partitioning in natural trachyte–trachyphonolite systems: insights from Campi Flegrei (southern Italy). Contrib. Mineral. Petrol. 158(3), 337-356. doi: 10.1007/s00410-009-0386-5

Gaetani GA (2004) The influence of melt structure on trace element partitioning near the peridotite solidus. Contrib. Mineral. Petrol. 147(5), 511-527.

Gaetani GA, Grove TL (1995) Partitioning of rare earth elements between clinopyroxene and silicate melt crystal-chemical controls. Geochimica et Cosmochimica Acta, 59(10), 1951-1962. https://doi.org/10.1016/0016-7037(95)00119-0

Griffin WL, Powell W, Pearson NJ, O'Reilly SY (2008) GLITTER: data reduction software for laser ablation ICP–MS. Laser Ablation–ICP–MS in the Earth Sciences vol. 40. Mineralogical Association of Canada Short Course Series, pp. 204-207

Hill E, Wood BJ, Blundy JD (2000) The effect of Ca-Tschermaks component on trace element partitioning between clinopyroxene and silicate melt. Lithos, 53(3), 203-215. https://doi.org/10.1016/S0024-4937(00)00025-6

Hill E, Blundy JD. Wood BJ (2011) Clinopyroxene–melt trace element partitioning and the development of a predictive model for HFSE and Sc. Contrib. Mineral. Petrol. 161(3), 423-438. doi: 10.1007/s00410-010-0540-0

Hornig-Kjarsgaard, I. (1998) Rare earth elements in sövitic carbonatites and their mineral phases. Journal of Petrology, 39(11-12), 2105-2121.

Huang F, Lundstrom CC, McDonough WF (2006) Effect of melt structure on trace-element partitioning between clinopyroxene and silicic, alkaline, aluminous melts. American Mineralogist, 91(8-9), 1385-1400. https://doi.org/10.2138/am.2006.1909

Keller J, Krafft M (1990) Effusive natrocarbonatite activity of Oldoinyo Lengai, June 1988. Bulletin of Volcanology, 52(8), 629-645.

Lundstrom CC, Shaw HF, Ryerson FJ, Phinney DL, Gill JB, Williams Q (1994) Compositional controls on the partitioning of U, Th, Ba, Pb, Sr and Zr between clinopyroxene and haplobasaltic melts: implications for uranium series disequilibria in basalts. Earth and Planetary Science Letters, 128(3-4), 407-423.

McDonough WF, Sun SS (1995). The composition of the Earth. Chemical geology, 120(3-4), 223-253.

Masotta M, Mollo S, Freda C, Gaeta M, Moore G (2013) Clinopyroxene–liquid thermometers and barometers specific to alkaline differentiated magmas. Contributions to Mineralogy and Petrology 166(6), 1545-1561. http://doi.org/10.1007/s00410-013-0927-9

Marks M, Halama R, Wenzel T, Markl G (2004) Trace element variations in clinopyroxene and amphibole from alkaline to peralkaline syenites and granites: implications for mineral–melt trace-element partitioning. Chemical geology, 211(3), 185-215. https://doi.org/10.1016/j.chemgeo.2004.06.032

Martin LH, Schmidt MW, Mattsson HB, Guenther D (2013) Element partitioning between immiscible carbonatite and silicate melts for dry and H_2O-bearing systems at 1–3 GPa. Journal of Petrology, 54(11), 2301-2338.

Michely LT, Leitzke FP, Speelmanns IM, Fonseca ROC (2017) Competing effects of crystal chemistry and silicate melt composition on trace element behavior in magmatic systems: insights from crystal/silicate melt partitioning of the REE, HFSE, Sn, In, Ga, Ba, Pt and Rh. Contributions to Mineralogy and Petrology, 172(6), 39.

Möller V, Williams-Jones AE (2016) Petrogenesis of the Nechalacho Layered Suite, Canada: magmatic evolution of a REE–Nb-rich nepheline syenite intrusion. Journal of Petrology, 57(2), 229-276. https://doi.org/10.1093/petrology/egw003

Mollex G, Füri E, Burnard P, Zimmermann L, Chazot G, Kazimoto EO, Marty B, France L (2018) Tracing helium isotope compositions from mantle source to fumaroles at Oldoinyo Lengai volcano, Tanzania. Chemical Geology 480(5), 66-74.

Mollex G (2017) Architecture de la plomberie du volcan carbonatitique Oldoinyo Lengai: nouvelles contraintes sur la source, les transferts hydrothermaux, et la différenciation magmatique dans la chambre active (PhD thesis, Université de Lorraine)

Mollo S, Putirka K, Misiti V, Soligo M, Scarlato P (2013) A new test for equilibrium based on clinopyroxene-melt pairs: Clues on the solidification temperatures of Etnean alkaline melts at post eruptive conditions. Chemical Geology 352, 92–100. http://dx.doi.org/10.1016/j.chemgeo.2013.05.026

Mollo S, Forni F, Bachmann O, Blundy JD, De Astis G, Scarlato P (2016) Trace element partitioning between clinopyroxene and trachy-phonolitic melts: A case study from the Campanian Ignimbrite (Campi Flegrei, Italy). Lithos, 252, 160-172. https://doi.org/10.1016/j.lithos.2016.02.024

Mollo S, Blundy J, Scarlato P, De Cristofaro SP, Tecchiato V, Di Stefano F, Vetere Bachmann O (2018) An integrated P-T-H_2O-lattice strain model to quantify the role of clinopyroxene fractionation on REE+ Y and HFSE patterns of mafic alkaline magmas: Application to eruptions at Mt. Etna. Earth-Science Reviews, 185, 32-56.

Morimoto N (1988) Nomenclature of pyroxenes. Mineralogy and Petrology, 39(1), 55-76.

Nagasawa H (1966) Trace element partition coefficient in ionic crystals. Science, 152(3723), 767-769.

Olin PH, Wolff JA (2010) Rare earth and high field strength element partitioning between iron-rich clinopyroxenes and felsic liquids. Contrib. Mineral. Petrol. 160(5), 761-775. doi: 10.1007/s00410-010-0506-2

Onuma N, Higuchi H, Wakita H, Nagasawa H (1968) Trace element partition between two pyroxenes and the host lava. Earth and Planetary Science Letters, 5, 47-51. https://doi.org/10.1016/S0012-821X(68)80010-X

Reguir EP, Chakhmouradian AR, Pisiak L, Halden NM, Yang P, Xu C, Kynicky J, Couëslan CG (2012) Trace-element composition and zoning in clinopyroxene-and amphibole-group minerals: implications for element partitioning and evolution of carbonatites. Lithos, 128, 27-45. https://doi.org/10.1016/j.lithos.2011.10.003

Shannon RD (1976) Revised effective ionic radii and systematic studies of interatomic distances in halides and chalcogenides. Acta crystallographica section A: crystal physics, diffraction, theoretical and general crystallography, 32(5), 751-767.

Vuorinen JH, Hålenius U, Whitehouse MJ, Mansfeld J, Skelton AD (2005) Compositional variations (major and trace elements) of clinopyroxene and Ti-andradite from pyroxenite, ijolite and nepheline syenite, Alnö Island, Sweden. Lithos, 81(1-4), 55-77. https://doi.org/10.1016/j.lithos.2004.09.021

Weidendorfer D, Schmidt MW, Mattsson HB (2016) Fractional crystallization of Si-undersaturated alkaline magmas leading to unmixing of carbonatites on Brava Island (Cape Verde) and a general model of carbonatite genesis in alkaline magma suites. Contrib. Mineral. Petrol. 171(5), 43. doi: 10.1007/s00410-016-1249-5

Wood BJ, Blundy JD (2001) The effect of cation charge on crystal–melt partitioning of trace elements. Earth and Planetary Science Letters, 188(1-2), 59-71.

Wood BJ, Blundy JD (1997) A predictive model for rare earth element partitioning between clinopyroxene and anhydrous silicate melt. Contrib. Mineral. Petrol. 129(2-3), 166-181.

Wood BJ, Blundy JD (2007) Trace element partitioning under crustal and uppermost mantle conditions: the influences of ionic radius, cation charge, pressure, and temperature. Treatise on Geochemistry, 2, 568.

Woodland AB, Jugo PJ (2007). A complex magmatic system beneath the Deves volcanic field, Massif Central, France: evidence from clinopyroxene megacrysts. Contributions to Mineralogy and Petrology, 153(6), 719-731.

Yang, X. M., Yang, X. Y., Chen, T. H., Zhang, P. S., Tao, K. J., Le Bas, M. J., Henderson, P. (2000) Geochemical characteristics of a carbonatite dyke rich in rare earths from Bayan Obo, China.

Zhang C, Koepke J, France L, Godard M (2017) Felsic Plutonic Rocks from IODP Hole 1256D, Eastern Pacific: Implications for the Nature of the Axial Melt Lens at Fast-Spreading Mid-Ocean Ridges. Journal of Petrology, 58(8), 1535-1565. doi: 10.1093/petrology/egx064

847 Tables

848

Table 1. Partition coefficients (*D*) between Cpx and phonolite melt.

	D	*σ*
Rb	0.0001	0.00003
Ba	0.0002	0.0001
Li	0.80	0.2
Th	0.0003	0.0001
Ta	0.0016	0.001
Nb	0.0003	0.0001
La	0.013	0.005
Ce	0.018	0.0076
Pr	0.029	0.011
Sr	0.659	0.233
Nd	0.041	0.01
Hf	0.247	0.10
Zr	0.134	0.06
Sm	0.062	0.02
Eu	0.062	0.01
Gd	0.063	0.02
Ti	0.314	0.16
Tb	0.064	0.02
Dy	0.056	0.01
Ho	0.063	0.02
Er	0.074	0.03
Tm	0.122	0.05
Yb	0.219	0.09
Lu	0.412	0.14
Sc	1.092	0.39
V	0.627	0.33
Ge	0.824	0.49
Al	0.034	0.01
Na	0.165	0.02
Mn	1.152	0.52
K	0.002	0.001

849

850

Table 2. Lattice strain parameters for trivalent and tetravalent cations (Cpx-phonolite, Oldoinyo Lengai).

	M1 site				M2 site			
	mean	σ	min	max	mean	σ	min	max
D_0^{3+}	1.240	0.441	0.62	1.92	0.07	0.015	0.05	0.09
E^{3+}	382	48	295	459	390	34	325	441
r_0^{3+}	0.740	0.006	0.73	0.75	1.05	0.017	1.01	1.07
D_0^{4+}	0.896	0.116	0.73	1.08				
E^{4+}	2071	213	1736	2397				
r_0^{4+}	0.658	0.002	0.655	0.662				

851

Fig 1

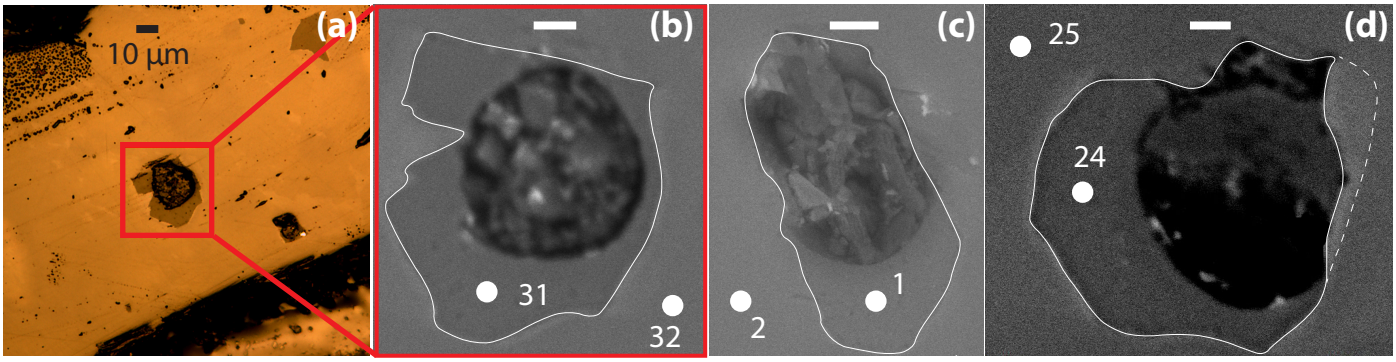

Fig 2

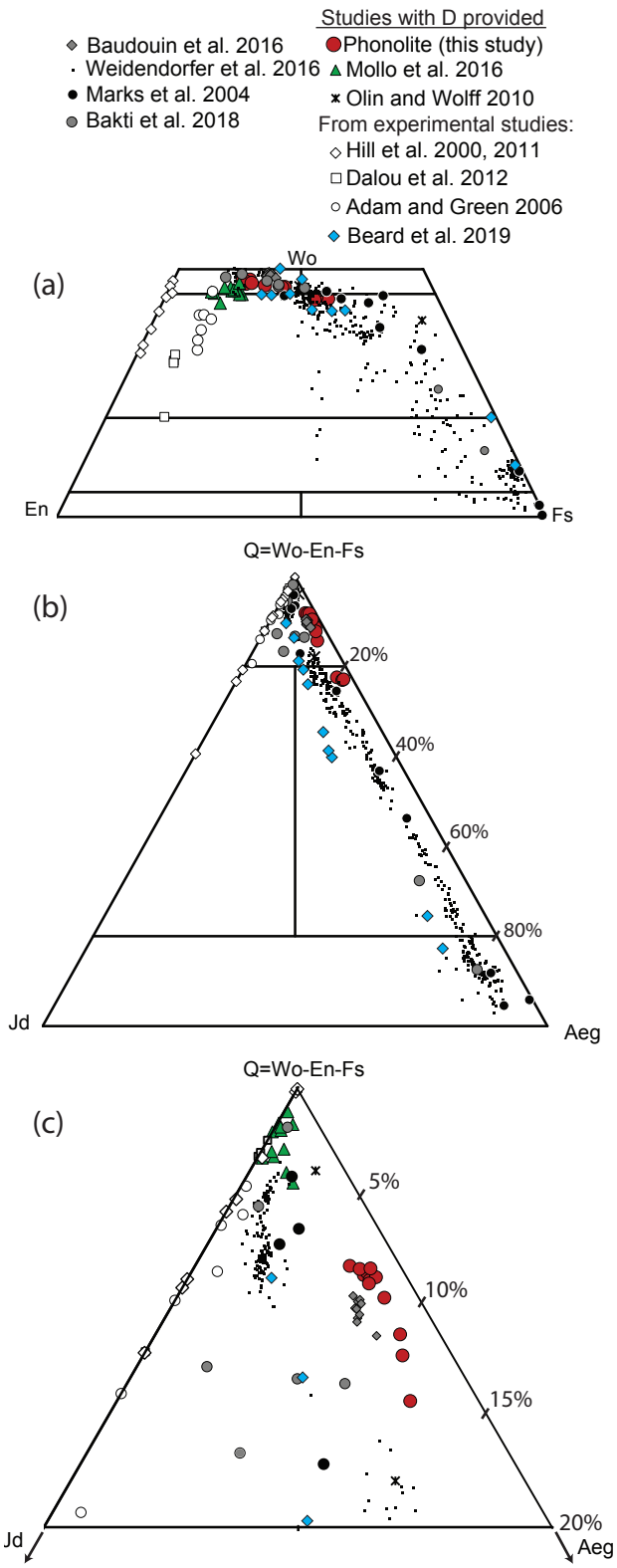
Studies with D provided
Baudouin et al. 2016
Weidendorfer et al. 2016
Marks et al. 2004
Bakti et al. 2018
Phonolite (this study)
Mollo et al. 2016
Olin and Wolff 2010
From experimental studies:
Hill et al. 2000, 2011
Dalou et al. 2012
Adam and Green 2006
Beard et al. 2019
(a)
Wo
En
Fs
Q=Wo-En-Fs
(b)
20%
40%
60%
80%
Jd
Aeg
Q=Wo-En-Fs
(c)
5%
10%
15%
20%
Jd
Aeg

Fig 3

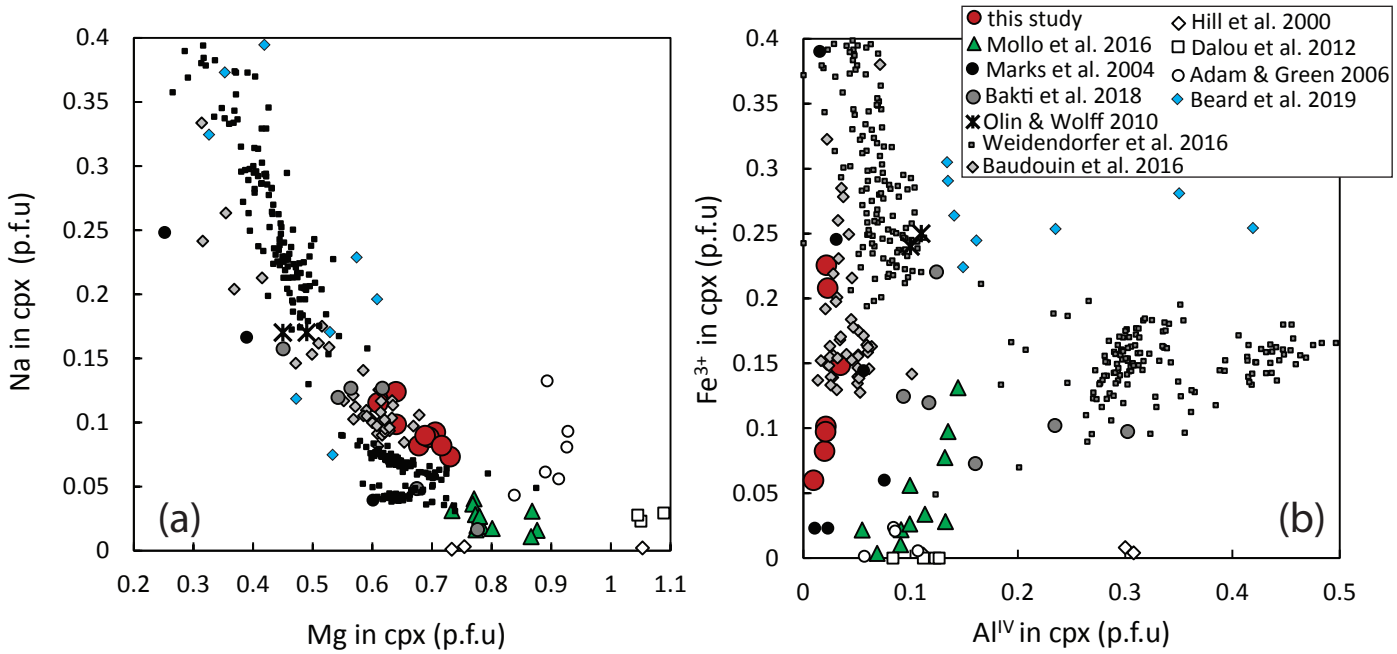
this study
Mollo et al. 2016
Marks et al. 2004
Bakti et al. 2018
Olin & Wolff 2010
Weidendorfer et al. 2016
Baudouin et al. 2016
Hill et al. 2000
Dalou et al. 2012
Adam & Green 2006
Beard et al. 2019
(a)
(b)
Na in cpx (p.f.u)
Mg in cpx (p.f.u)
Fe3+ in cpx (p.f.u)
AlIV in cpx (p.f.u)

Fig 4

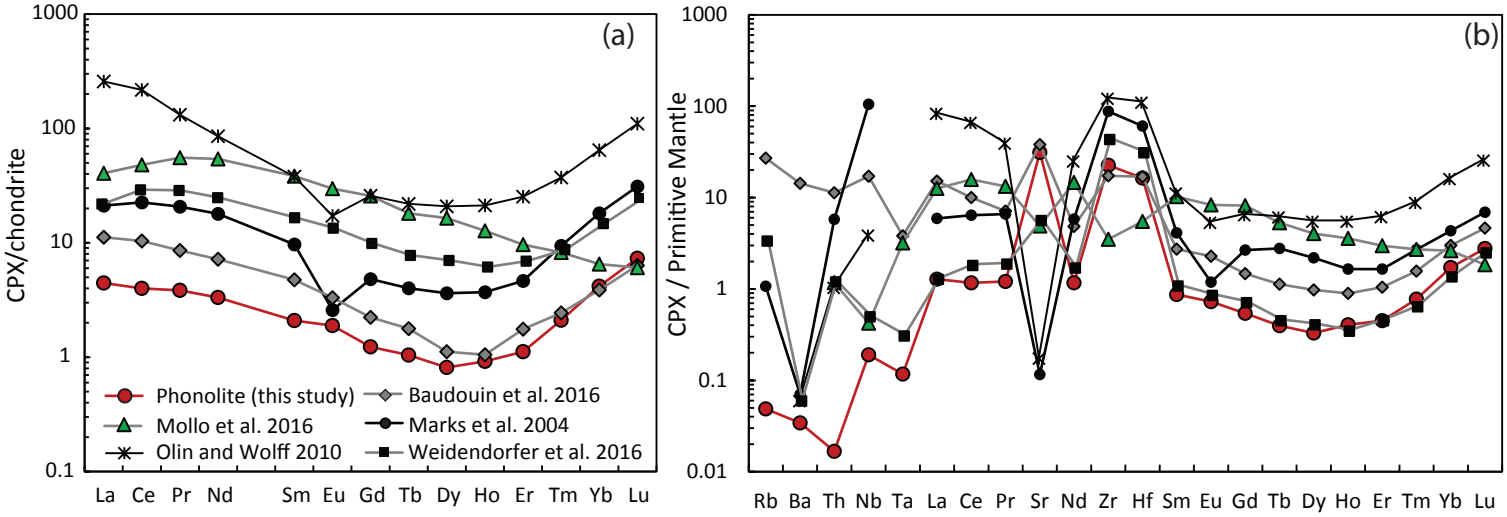
(a)
CPX/chondrite
1000
100
10
1
0.1
La Ce Pr Nd Sm Eu Gd Tb Dy Ho Er Tm Yb Lu
Phonolite (this study)
Baudouin et al. 2016
Mollo et al. 2016
Marks et al. 2004
Olin and Wolff 2010
Weidendorfer et al. 2016
(b)
CPX / Primitive Mantle
1000
100
10
1
0.1
0.01
Rb Ba Th Nb Ta La Ce Pr Sr Nd Zr Hf Sm Eu Gd Tb Dy Ho Er Tm Yb Lu

Fig 5

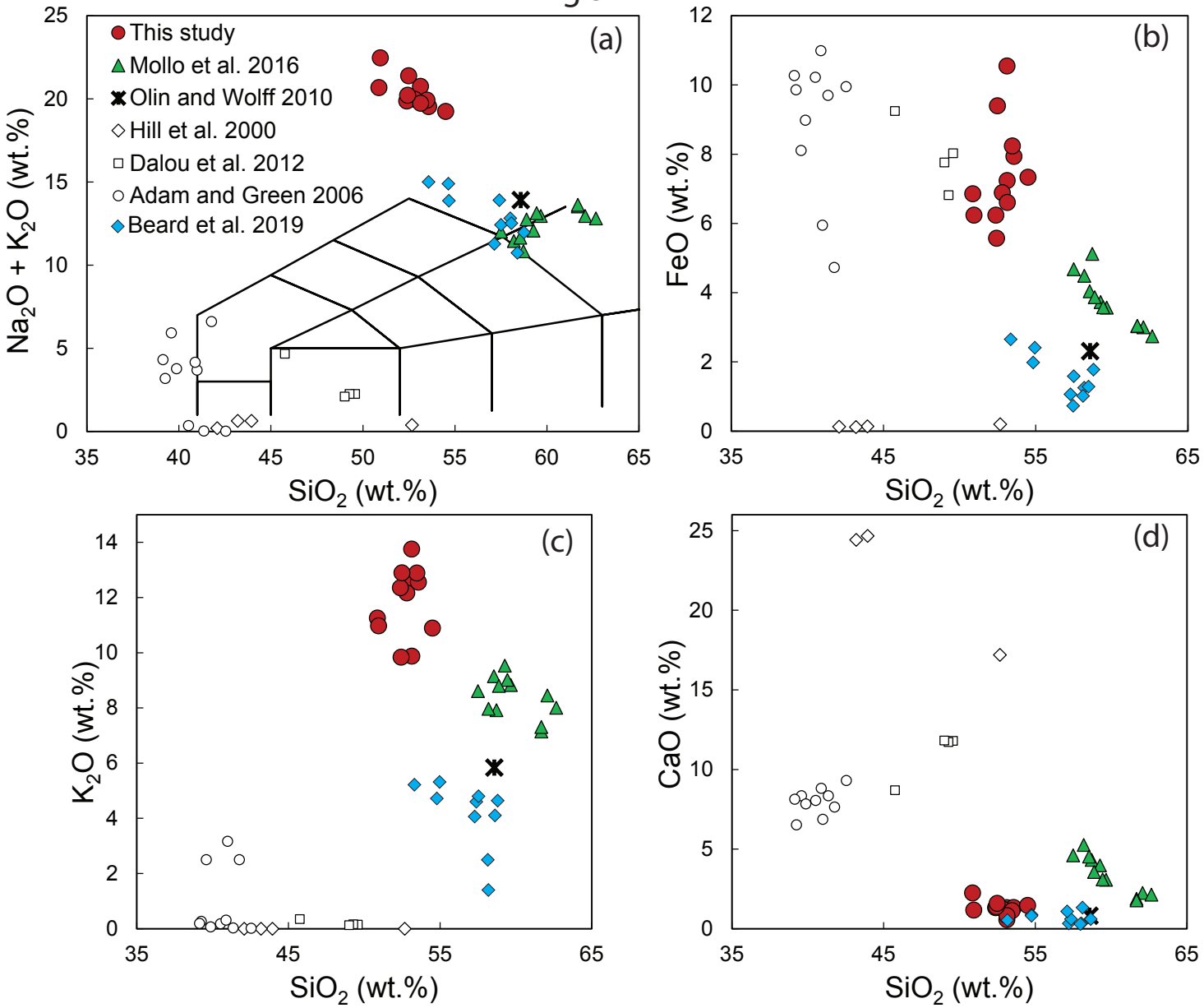
This study
Mollo et al. 2016
Olin and Wolff 2010
Hill et al. 2000
Dalou et al. 2012
Adam and Green 2006
Beard et al. 2019
(a)
(b)
(c)
(d)
Na2O + K2O (wt.%)
FeO (wt.%)
K2O (wt.%)
CaO (wt.%)
SiO2 (wt.%)

Fig 6

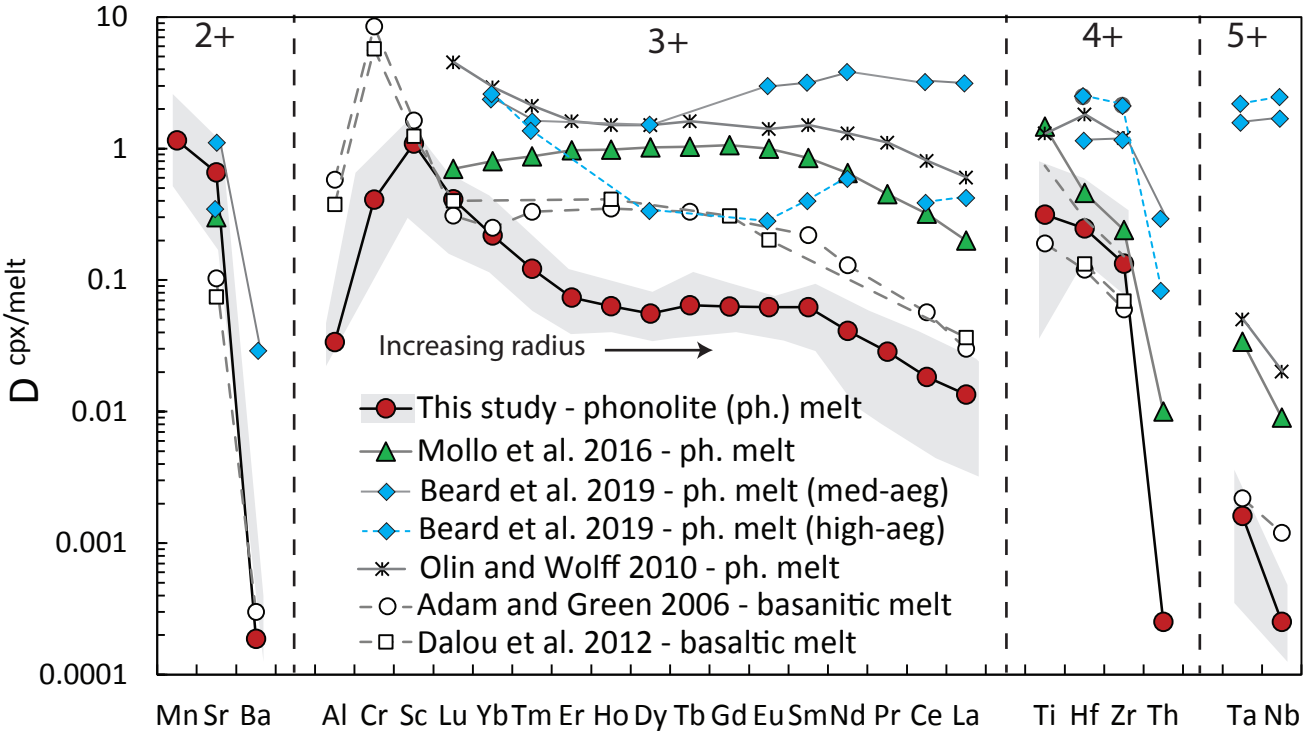
10
1
0.1
0.01
0.001
0.0001
D cpx/melt
2+
3+
4+
5+
Increasing radius
This study - phonolite (ph.) melt
Mollo et al. 2016 - ph. melt
Beard et al. 2019 - ph. melt (med-aeg)
Beard et al. 2019 - ph. melt (high-aeg)
Olin and Wolff 2010 - ph. melt
Adam and Green 2006 - basanitic melt
Dalou et al. 2012 - basaltic melt
Mn Sr Ba
Al Cr Sc Lu Yb Tm Er Ho Dy Tb Gd Eu Sm Nd Pr Ce La
Ti Hf Zr Th
Ta Nb

Fig 7

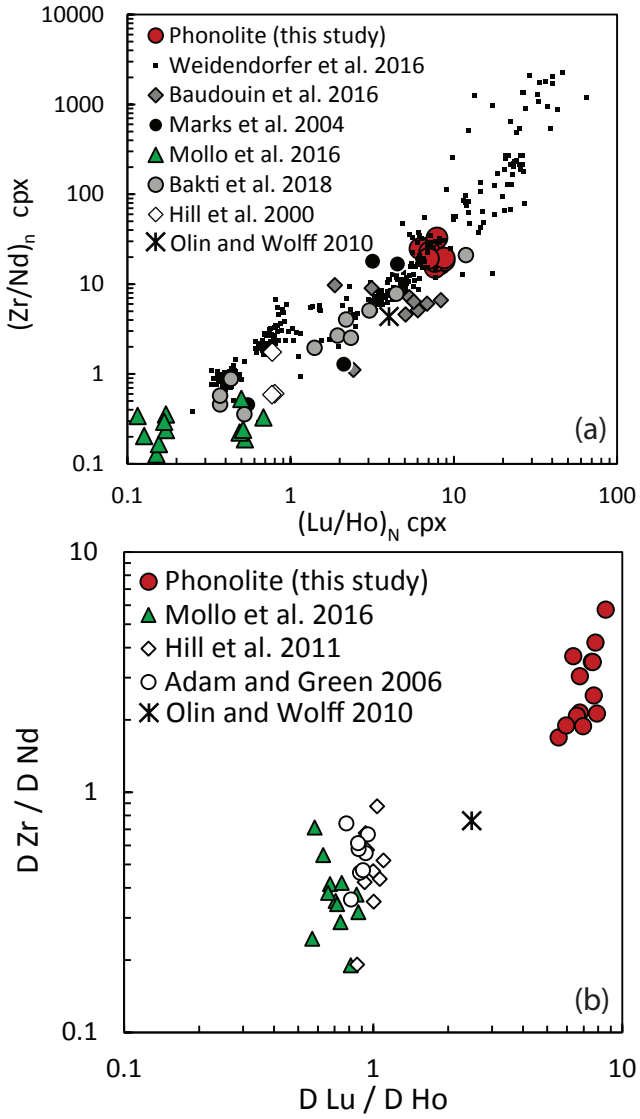
Phonolite (this study)
Weidendorfer et al. 2016
Baudouin et al. 2016
Marks et al. 2004
Mollo et al. 2016
Bakti et al. 2018
Hill et al. 2000
Olin and Wolff 2010
(Zr/Nd)n cpx
(Lu/Ho)N cpx
(a)
Phonolite (this study)
Mollo et al. 2016
Hill et al. 2011
Adam and Green 2006
Olin and Wolff 2010
D Zr / D Nd
D Lu / D Ho
(b)

Fig 8

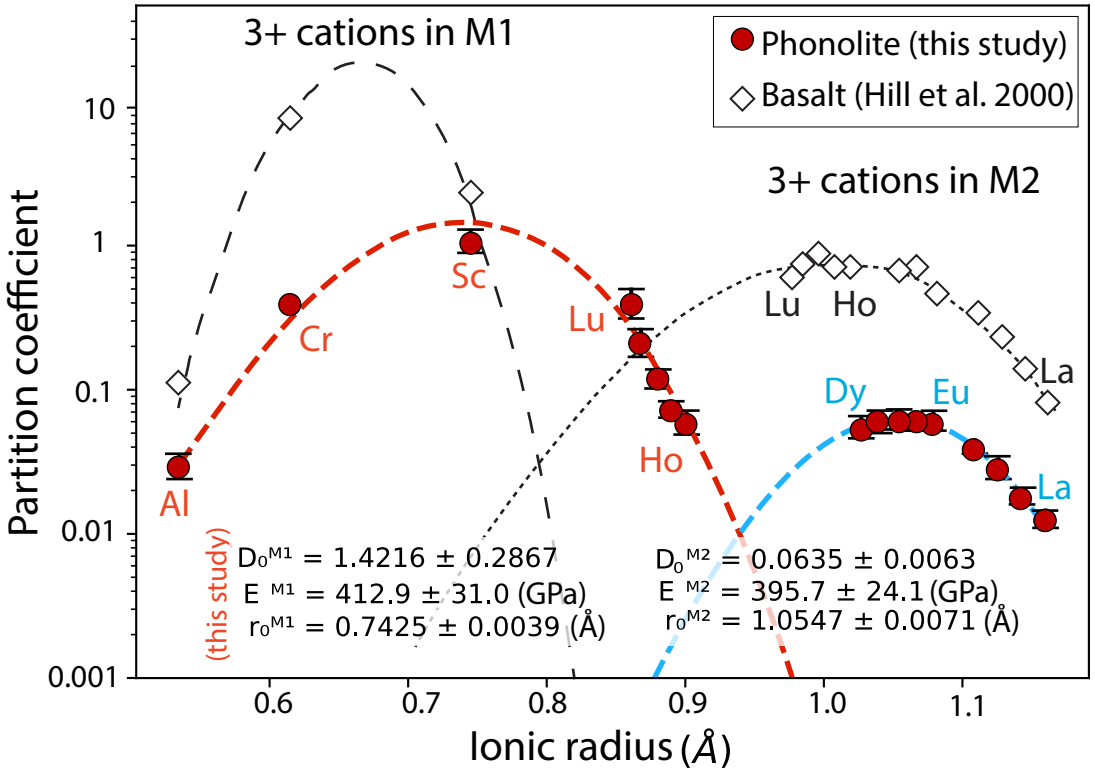
3+ cations in M1
Phonolite (this study)
Basalt (Hill et al. 2000)
3+ cations in M2
Partition coefficient
10
1
0.1
0.01
0.001
Sc
Cr
Lu
Al
Ho
Lu
Ho
La
Dy
Eu
La
(this study)
D₀M1 = 1.4216 ± 0.2867
E M1 = 412.9 ± 31.0 (GPa)
r₀M1 = 0.7425 ± 0.0039 (Å)
D₀M2 = 0.0635 ± 0.0063
E M2 = 395.7 ± 24.1 (GPa)
r₀M2 = 1.0547 ± 0.0071 (Å)
0.6
0.7
0.8
0.9
1.0
1.1
Ionic radius (Å)

Fig 9

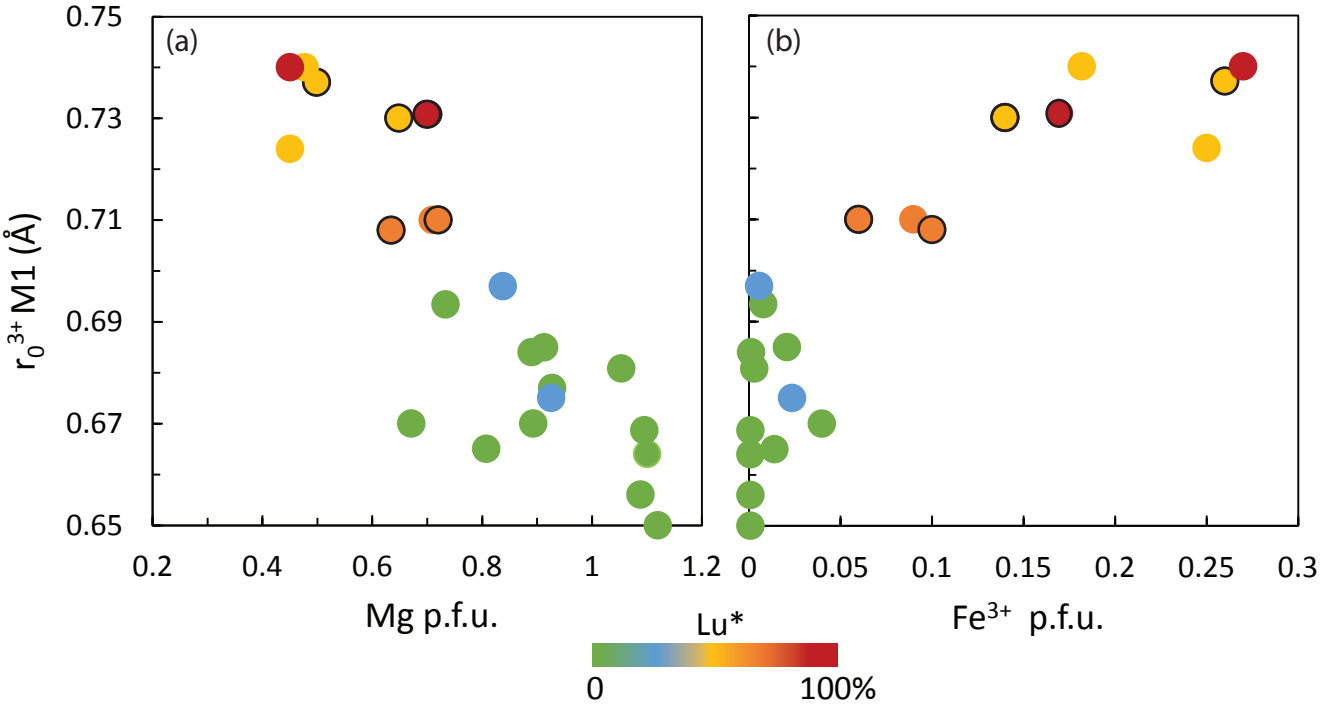
(a)
(b)
0.75
0.73
0.71
0.69
0.67
0.65
r_0^{3+} M1 (Å)
0.2
0.4
0.6
0.8
1
1.2
Mg p.f.u.
0
0.05
0.1
0.15
0.2
0.25
0.3
Fe^{3+} p.f.u.
Lu*
0
100%

Fig 10

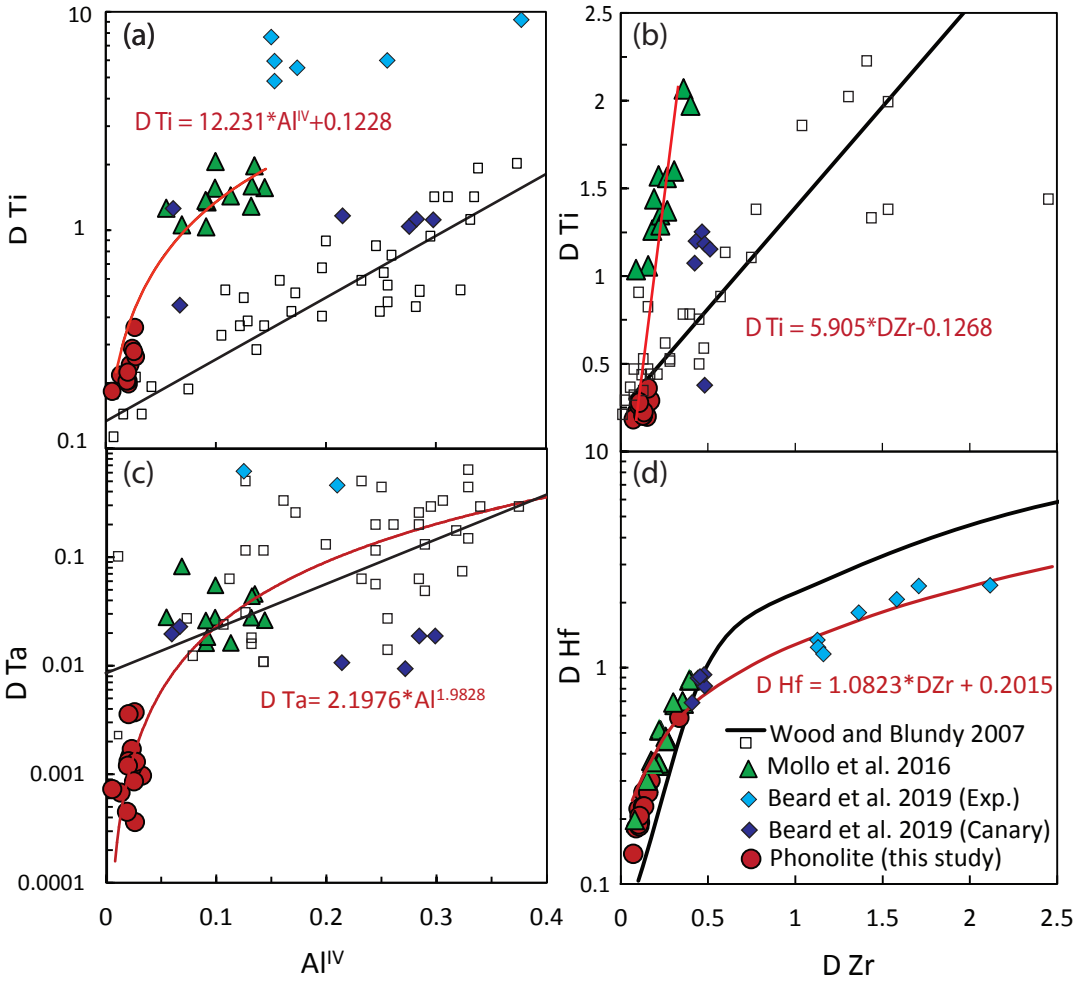
(a)
D Ti = 12.231*AlIV+0.1228
D Ti
(b)
D Ti = 5.905*DZr-0.1268
D Ti
(c)
D Ta= 2.1976*Al1.9828
D Ta
AlIV
(d)
D Hf = 1.0823*DZr + 0.2015
D Hf
D Zr
Wood and Blundy 2007
Mollo et al. 2016
Beard et al. 2019 (Exp.)
Beard et al. 2019 (Canary)
Phonolite (this study)

Figure 11

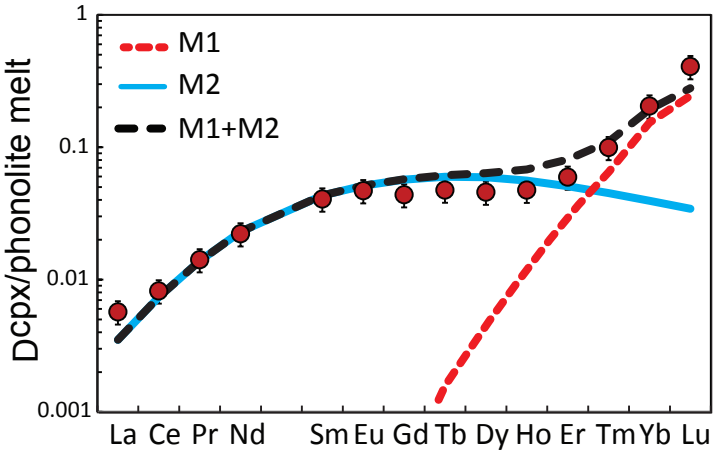
M1
M2
M1+M2
Dcpx/phonolite melt
1
0.1
0.01
0.001
La Ce Pr Nd Sm Eu Gd Tb Dy Ho Er Tm Yb Lu

Fig 12

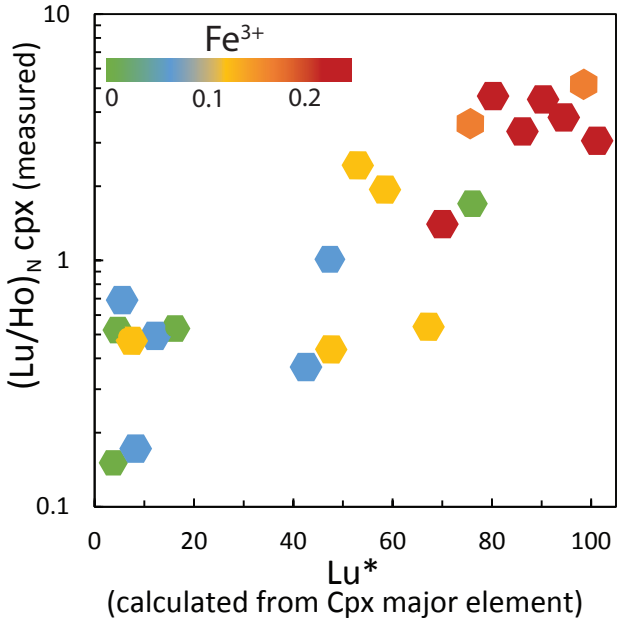
Fe3+
0
0.1
0.2
10
1
0.1
(Lu/Ho)N cpx (measured)
0
20
40
60
80
100
Lu*
(calculated from Cpx major element)

Fig 13

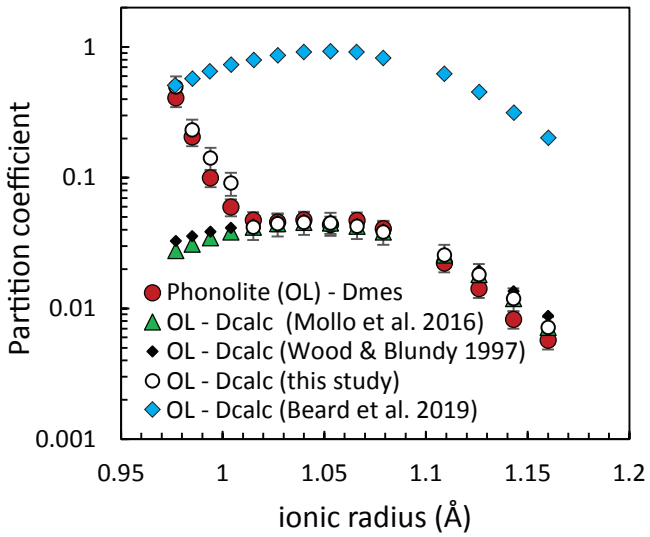
Partition coefficient
1
0.1
0.01
0.001
0.95
1
1.05
1.1
1.15
1.2
ionic radius (Å)
Phonolite (OL) - Dmes
OL - Dcalc (Mollo et al. 2016)
OL - Dcalc (Wood & Blundy 1997)
OL - Dcalc (this study)
OL - Dcalc (Beard et al. 2019)

Figure 14

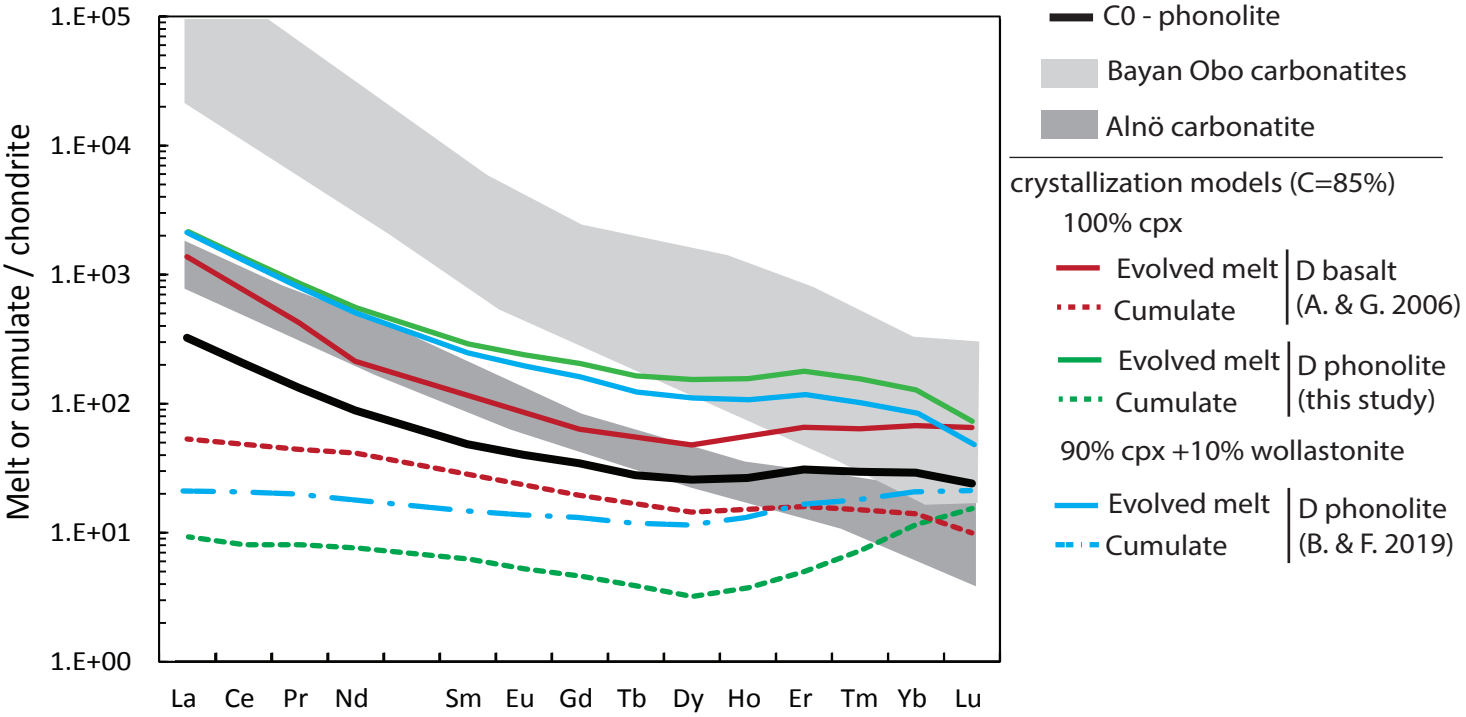
1.E+05
1.E+04
1.E+03
1.E+02
1.E+01
1.E+00
Melt or cumulate / chondrite
La
Ce
Pr
Nd
Sm
Eu
Gd
Tb
Dy
Ho
Er
Tm
Yb
Lu
C0 - phonolite
Bayan Obo carbonatites
Alnö carbonatite
crystallization models (C=85%)
100% cpx
Evolved melt
Cumulate
D basalt
(A. & G. 2006)
Evolved melt
Cumulate
D phonolite
(this study)
90% cpx +10% wollastonite
Evolved melt
Cumulate
D phonolite
(B. & F. 2019)